APPENDIX D

SUMMARY OF RECENT INFORMATION RELEVANT TO THE ENGINEERED BARRIER SYSTEM DEGRADATION, FLOW, AND TRANSPORT PROCESS MODEL

INTENTIONALLY LEFT BLANK

SUMMARY OF RECENT INFORMATION RELEVANT TO THE ENGINEERED BARRIER SYSTEM DEGRADATION, FLOW, AND TRANSPORT PROCESS MODEL

1. INTRODUCTION

This white paper contains a summary of recent test results and other additional information that is relevant to the engineered barrier system (EBS) degradation, flow, and transport process model used to support the *Yucca Mountain Science and Engineering Report* (YMS&ER) (DOE 2001a) and the *Yucca Mountain Preliminary Site Suitability Evaluation* (YMPSSE) (DOE 2001b). The U.S. Department of Energy (DOE) released these two documents for public review in May and August, respectively, of this year.

The white paper focuses on the results of those field and laboratory tests and other additional information that became available after the EBS process model was completed to support the preparation of the YMS&ER and the YMPSSE. The summary of this recent information is being used to conduct an impact review, in accordance with AP-2.14Q, *Review of Technical Products and Data*, to determine if this additional information has any impact on the technical analyses supporting the YMS&ER and the YMPSSE. The documentation of the additional information in this white paper is an interim step and primarily used to support this impact review. This information is expected to be formally documented in subsequent Project technical reports, as appropriate.

To assist in the impact review, this white paper briefly describes the EBS process model that was used to support the YMS&ER and the YMPSSE, provides a summary of the recent test results and other additional information, and discusses the potential implications of this more recent information on our understanding of the EBS process model.

2. SUMMARY DESCRIPTION OF THE EBS PROCESS MODEL

The EBS process model calculates the flow of water through the EBS, including the effects on the water chemistry of interactions with natural and engineered components, and on transport of radionuclides released from the waste form. The model (which is really a sequence of models) also calculates the degradation of the emplacement drifts over time due to gravitational loads, thermal effects, and seismic motion. The model includes evaluation of features, events and processes in *Engineered Barrier System Features, Events, and Processes* (CRWMS M&O 2001a). It also includes abstractions, which simplify model results for inclusion in the total system model while retaining process dependencies.

Figures 1 and 2 show the sequence of process models used to track the water (hydraulics models) and the water and gas chemistry (chemical models). Table 1 summarizes the drift degradation models (not shown in the two figures) (1) used in the total system performance assessment—site recommendation (TSPA-SR) model documented in *Total System Performance Assessment for the Site Recommendation* (CRWMS M&O 2000a) and (2) used in the supplemental TSPA model documented in *FY01 Supplemental Science and Performance Analyses* (BSC 2001a). Tables 2 and 3 summarize the hydraulics and chemical models, respectively, shown in the two figures.

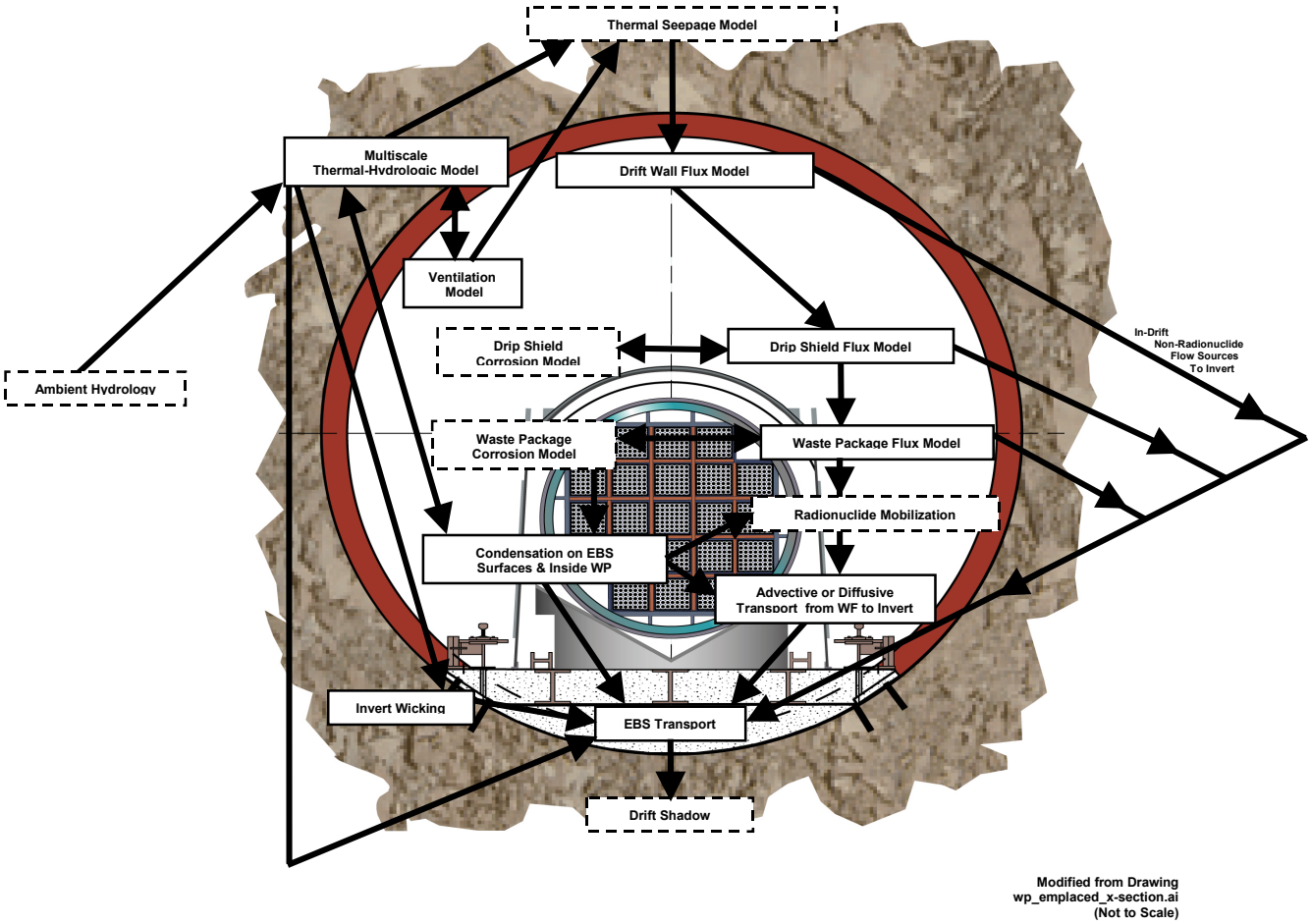

Figure 1. EBS Hydraulics Model Sequence

Figure 1 includes hydraulics process models within the EBS group of models, as well as some models that directly interface with the EBS models (shown in dashed boxes). Table 2 summarizes the state of the hydraulics models in performance assessments for site recommendation and notes additional data obtained or modeling done since the *FY01 Supplemental Science and Performance Analyses* (BSC 2001a). A key point in the hydraulics model is that most of the water entering the drift will not contact the waste form, as shown by the multiple opportunities for seepage to bypass the waste package interior. Seepage can reach the invert as film flow along the drift wall, outside of the drip shield, inside of the drip shield, and outside of the waste package, and by dripping outside the drip shield or waste package. Additional water can reach the invert by wicking from the host rock and by condensation on cool surfaces. The hydraulics modeling is conservative in both the TSPA-SR model and supplemental TSPA model, in that more water is modeled as reaching the waste package interior than would be expected in the repository. The supplemental TSPA model results in less water reaching the waste package interior than the TSPA-SR model.

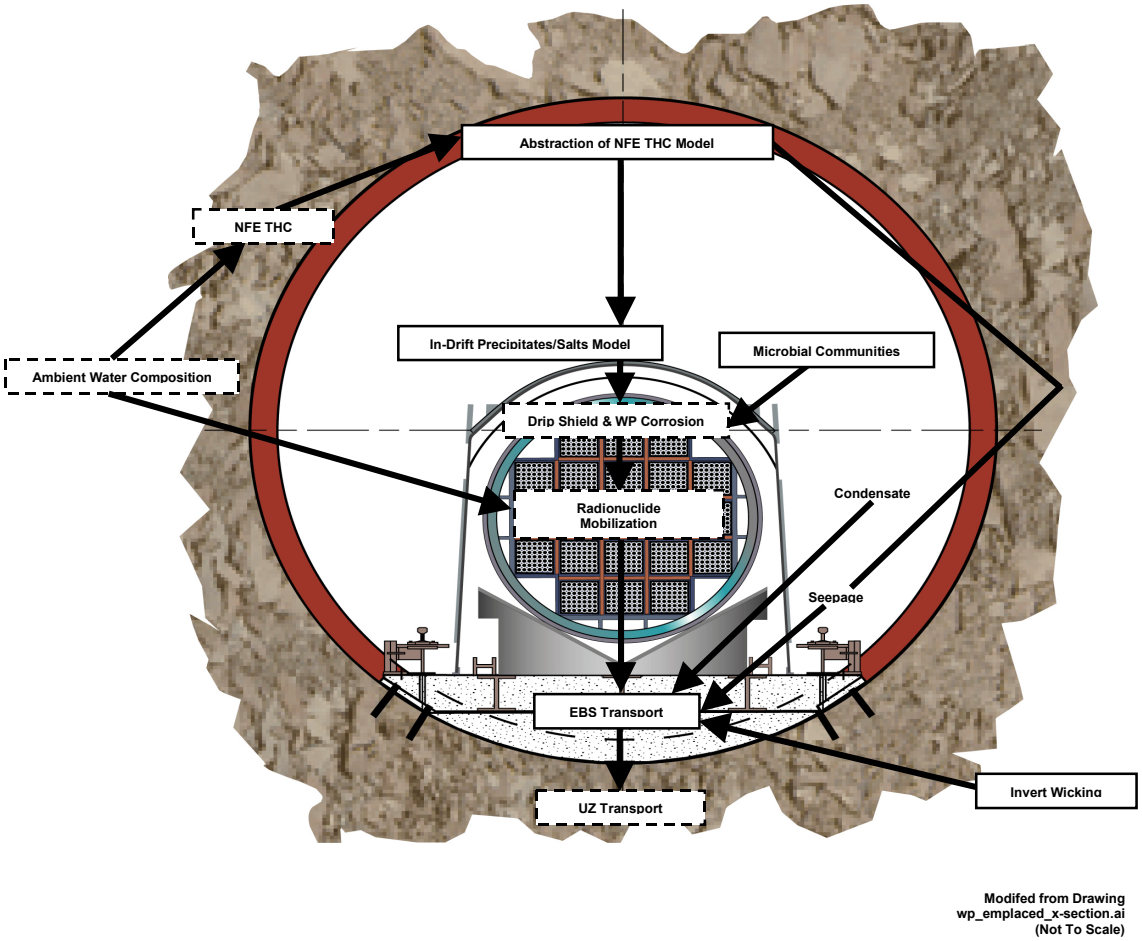

Figure 2. Supplemental TSPA Model EBS Chemical Models

Table 1. EBS Model Summary, Drift Degradation Models

Model	TSPA-SR Model Summary	Supplemental TSPA Model Summary	TSPA-Level or Subsystem-Level Use in Supplemental Model	Additional Information in Section 3 of this White Paper
Drift Degradation	Key Block Analysis, thermal and seismic effects, four host rock units	Sensitivity analyses to examine importance of fracture length, sub-horizontal fractures, and fracture variability	Subsystem	No
Rockfall on Drip Shield and Waste Package	Effect of rockfall and drift deformation on EBS performance screened out	No change	N/A	3.1

Table 2. EBS Model Summary, Hydraulics Models

Model	TSPA-SR Model Summary	Supplemental Model Summary	TSPA-level or Subsystem-level Use in Supplemental Model	Additional Information in Section 3 of this White Paper
Ambient Hydrology	Input from the unsaturated zone flow and transport model			
Ventilation Model	Heat removal efficiency based on conduction-only heat transfer	Latent heat, near-field dryout, and mass transfer considered	Subsystem	3.2, 3.3, 3.4
Multiscale Thermal-Hydrologic Model	2D TH column submodels modified by 3D mountain scale & drift scale temperature-only submodels to account for stratigraphy, infiltration variability, footprint, and waste package power variability. Includes invert evaporation	Improved in-drift radiation and mass transfer aspects, investigated sensitivity to lithophysal porosity, conductivity, ventilation efficiency, and temporal dependence of ventilation efficiency	TSPA except for sensitivity studies	3.5, 3.6
Thermal Seepage Model	Interface with the unsaturated zone flow and model			
Drift Wall Flux Model	All seepage assumed to drip, and all drips assumed to fall on drip shield	No change	TSPA	No
Drip Shield Corrosion Model	Interface with the waste package degradation model			
Drip Shield Flux Model	Flow through breaches based on breach area vs drip shield area. All flow through breaches assumed to drip, and all drips assumed to fall on waste package	More realistic model with less “uphill” flow	TSPA	No
Waste Package Flux Model	Flow through breaches based on breach area vs waste package area	More realistic model with less “uphill” flow	TSPA	No
Waste Package Corrosion Model	Interface with the waste package degradation model			
Radionuclide Mobilization Model	Interface with the waste form degradation white paper model			
Advective or Diffusive Release from WF to Invert	Diffusion through breach in Alloy 22	Diffusion within waste package and through breach	TSPA	No
Condensation Model	No condensation in drift, except from multiscale thermal-hydrologic model	Condensation at drip shield locations cooler than invert, quantity set by invert evaporation rate	Subsystem	3.7, 3.12
Invert Wicking	Hydrologic equilibration between host rock and invert gravel (single continuum gravel model)	No change	N/A	3.8
EBS Transport	Advection and diffusion in invert gravel	Changes were in chemical aspects (see Table 3)	N/A	3.9
Drift Shadow	Output to the unsaturated zone flow and transport model			

Figure 2, the chemical models, also shows EBS process models and models that directly interface with the EBS models. Table 3 summarizes the state of the chemical models in performance assessments for site recommendation and notes additional data obtained or modeling done since *FY01 Supplemental Science and Performance Analyses* (BSC 2001a). The supplemental TSPA model of the invert was more realistic than TSPA-SR since it included chemical mixing of the invert water sources, sorption of radionuclides, and temperature-dependence.

Table 3. EBS Model Summary, Chemical Models

Model	TSPA-SR Model Summary	Supplemental TSPA Model Summary	TSPA-level or Subsystem-level Use in Supplemental Model	Additional Information in Section 3 of this White Paper
Ambient Water Composition	Input from the unsaturated zone flow and transport model			
NFE THC Model	Input from the unsaturated zone flow and transport model			
Abstraction of NFE THC Model	Chemistry averaged within time periods	Expanded set of time periods, increased variability, and conservation of charge balance	TSPA	3.10, 3.11
In-Drift Precipitates/Salts Model	Water chemistry equilibrated on EBS surfaces, including effects of evaporation and condensation	Includes uncertainty in composition of gas and liquid entering the drifts	TSPA	3.10
Microbial Communities Model	Include effects of original microbes, energy availability, and nutrient availability	Based on updated data	Subsystem	3.10
Drip Shield and Waste Package Corrosion Models	Interface with the waste package degradation models			
Waste Form Release Model	Interface with the waste form degradation model			
Condensation Model	See Table 2	Changes were in hydraulics aspects (see Table 2)	N/A	N/A
Invert Wicking	See Table 2	Changes were in hydraulics aspects (see Table 2)	N/A	N/A
EBS Transport	Advection and diffusion in invert gravel	Four source mixing model, sorption, and temperature dependence added	Subsystem	3.10
		Diffusion equation modified	TSPA	3.9
UZ Transport	Output to the unsaturated zone flow and transport model			

3. SUMMARY OF RECENT TEST RESULTS AND OTHER ADDITIONAL INFORMATION

This section summarizes recent results obtained from the field tests and modeling that have provided information relevant to enhancing our understanding of the EBS process models. The tests and modeling that provided this additional information are listed below and discussed in each of the sections that follow.

1. Analysis of rockfall effects on the drip shield and waste package
2. Comparison of heat transfer and heat/mass transfer models for preclosure ventilation
3. Computational fluid dynamics modeling of natural convection for 25-percent- and 44-percent-scale tests and at repository scale
4. Results of 25-percent-scale forced ventilation tests
5. Validation of the multiscale thermal-hydrologic model and corrections to supplemental TSPA model results
6. Thermal conductivity modeling and data at laboratory and field scales
7. Modeling of condensation on EBS surfaces
8. Dual-permeability modeling of the invert
9. Invert diffusion study
10. EBS physical and chemical environment model
11. Modeling of cement-seepage interactions
12. ECRB bulkhead test results

Because of the recent nature of the information provided in this section, much of it is unpublished and, therefore, some source references have been provided where appropriate, but others could not be provided. However, this information is currently documented in the principal investigators' scientific notebooks, if applicable, in accordance with the Project's quality assurance procedure AP-SIII.1Q, *Scientific Notebooks*.

3.1 ANALYSIS OF ROCKFALL EFFECTS ON THE DRIP SHIELD AND WASTE PACKAGE

An analysis (BSC 2001b) was performed to determine the structural performance of the drip shield under two rockfall design basis events (pointed rock and flat, horizontal, rock surface) with rocks up to 52 metric tons. This analysis improves the preceding analysis (CRWMS M&O 2000b) by including temperature dependent material properties and drip shield corrosion. Potential design changes were included in the analysis; these changes would stiffen the drip shield and increase its clearance from the waste package. For example, the drip shield overall

height was raised by 300 mm (12 in.), to increase the minimum available gap between the drip shield and waste package from 80 mm (3 in.) to 380 mm (15 in.).

Results show that the drip shield immediate response to rockfall for both rockfall events does not include failure in the drip shield top plate for any of the rock sizes considered. In addition, based on the threshold stress value for stress corrosion crack initiation, several assessments were made on the potential for initiation of stress corrosion cracking due to residual stresses caused by rockfall.

For a rockfall event in which the horizontal side of a large rock impacts the drip shield top, the results indicate that the maximum residual stress intensity (the difference between the first and third principal stresses) in the drip shield top plate is 170 MPa. The average value of the stress intensity over the top plate in the region of contact is approximately half of the maximum value. At these stress levels, the drip shield top plate area that is impacted by the rock block could be susceptible to stress corrosion cracking subsequent to rockfall.

The consequence of a single stress corrosion crack in the drip shield is not significant with regard to seepage penetration, due to capillary effects and plugging. If multiple cracks join, a section of the drip shield could fail. However, an important feature of the drip shield design is that the top plate is supported not only by bulkheads approximately 1 m (3.3 ft) apart from each other but also with three longitudinal stiffeners, one at the center and two 225 mm (8.86 in.) apart from the center. Therefore, the maximum potential plate failure section size of the drip shield top plate due to stress corrosion cracking is less than 1 m × 0.2 m, and multiple connected cracks would be required. This result is a consequence of the fact that the maximum stresses occur at the top section of the drip shield top plate and the stiffeners are anticipated to remain intact due to their high strength and thickness.

In the case of a pointed-edge rockfall, the area of contact, and consequently, the surface area of the top plate susceptible to stress corrosion cracking, is smaller than the horizontal rockfall.

The results of the potential design changes and analyses further support the conclusion that the drip shield can be designed to survive the impacts of rockfall and preclude contact between the drip shield and the waste package for calculated rockfall events up to the design basis limit.

3.2 COMPARISON OF HEAT TRANSFER AND HEAT/MASS TRANSFER MODELS FOR PRECLOSURE VENTILATION

For the TSPA-SR model and the supplemental TSPA model, ANSYS (CRWMS M&O 1998) was used to model the preclosure ventilation period. The results of the ANSYS calculation were used to reduce the magnitude of the heat source in the multiscale thermal-hydrologic model during the preclosure period for TSPA-SR and supplemental TSPA calculations.

The ANSYS numerical heat transfer model is unable to account directly for latent heat and water mass flow effects caused by the presence of water and water vapor in the near-field host rock and drift. These effects are coupled with the heat generated by the radioactive decay of the waste packages and the air flow in forced ventilation. The latent heat exchange caused by the phase change between the liquid and vapor states of water tends to cool the near-field environment as well as dry out the near-field host rock. As the near-field host rock dries, its thermal

conductivity decreases. This effect is expected to create an "insulating skin" around the drift, hence higher temperature gradients in the near-field rock and higher temperatures from the edge of the dryout region inward toward the drift wall. This insulating skin drives temperatures in the opposite direction to the cooling effect of latent heat removal by vaporization of the near-field moisture into the air stream (i.e., evaporative cooling). The evaporative cooling effect was hypothesized to dominate the increased thermal gradient due to rock dryout. This would tend to lower the peak drift temperatures from those calculated using the ANSYS ventilation model.

To evaluate the hypothesis, a second ventilation model was implemented using MULTIFLUX Version 1.0 (BSC 2001c). This code, developed by the University of Nevada Reno under a cooperative agreement with the DOE, couples a lumped-parameter computational fluid dynamics code to the NUFT porous medium (rock) code (LLNL 1999) used in the multiscale thermal-hydrologic model. In MULTIFLUX, a series of NUFT calculations is used to develop a response surface relating heat and mass flux histories at the drift wall to the drift wall temperature and pressure histories. The computational fluid dynamics calculation of the in-drift air is iterated with the NUFT response surface until the two results are consistent at their interface. The results, as documented in *FY01 Supplemental Science and Performance Analyses* (BSC 2001a), showed overall lower temperatures than the ANSYS ventilation model, supporting the hypothesis. However, closer inspection of the implementation of the models in the two codes (ANSYS and MULFTIFLUX) revealed enough differences in input parameters that the supplemental TSPA model comparison of results was uncertain.

Subsequent to the supplemental TSPA analyses documented in *FY01 Supplemental Science and Performance Analyses* (BSC 2001a), the MULTIFLUX ventilation code was rerun, using inputs that were as close as possible to those in the earlier ANSYS calculations, and the results were compared. The MULTIFLUX temperatures shifted upwards (hotter) from the previous run, by 15° to 25°C (27° to 45°F), for the waste package and drift wall. This shift resulted in 5° to 10°C (9° to 18°F) warmer temperatures for the new MULTIFLUX run, compared to the ANSYS temperatures.

Both codes, MULTIFLUX and ANSYS, include simplifications to handle the difficult three-dimensional transient situation that involves both porous media and open air spaces. Prior to concluding that the moisture-ventilation coupling results in cooler repository temperatures, additional calculations were initiated to test the effects of the simplifications in each model. For ANSYS, the coarse axial mesh (100-m [330-ft]-long air elements) was refined to 25-m (82-ft)-long air elements. The results were similar to the original ANSYS results but still 5° to 10°C (9° to 18°F) cooler than the MULTIFLUX results that included latent heat effects and near-field rock dryout.

The MULTIFLUX software is currently being qualified within the DOE and University of Nevada quality assurance programs. As part of the qualification process, the code was exercised in sub-domains (rock and air) on situations for which analytic solutions exist (Carslaw and Jaeger 1959). Some of the sub-domain exercises were also conducted using the ANSYS numerical code and the NUFT numerical code (which is used in both the ventilation model implemented in MULTIFLUX and the multiscale thermal-hydrologic model). In each case, a single method of heat and/or mass transfer was isolated (i.e. radiation only, convection only, and conduction only). For various cases, the models were broken down further to investigate single

phenomena such as the calculated variation of the thermal conductivity based on varying host rock saturation in the NUFT calculation. The results of these sub-domain calculations were then compared to each other, and where applicable, to analytical solutions. The result of these exercises, summarized in Figure 3 and Table 4, was a "piece by piece" benchmarking of the ANSYS and MULTIFLUX codes as applied to the ventilation model.

Figure 3 shows four temperature histories out to 50 years, for a location 6 m (20 ft) horizontally from the drift centerline (3.25 m (10.7 ft) into the near-field rock). Each temperature history uses the same value for rock thermal conductivity. The ANSYS and NUFT code results are similar. Agreement with the analytical solution is good at early times, but the analytical solution is cooler at later times. The difference is attributed to different boundary conditions at the lateral edge of the domain. The analytical solution uses a constant temperature at a boundary located an infinite distance away from the drift. The numerical models use an adiabatic (no heat flow) boundary at the locations corresponding to the water table and ground surface. Hence, as time progresses and heat flow reaches the boundary of the numerical models, their temperatures increase compared to the infinite analytical solution.

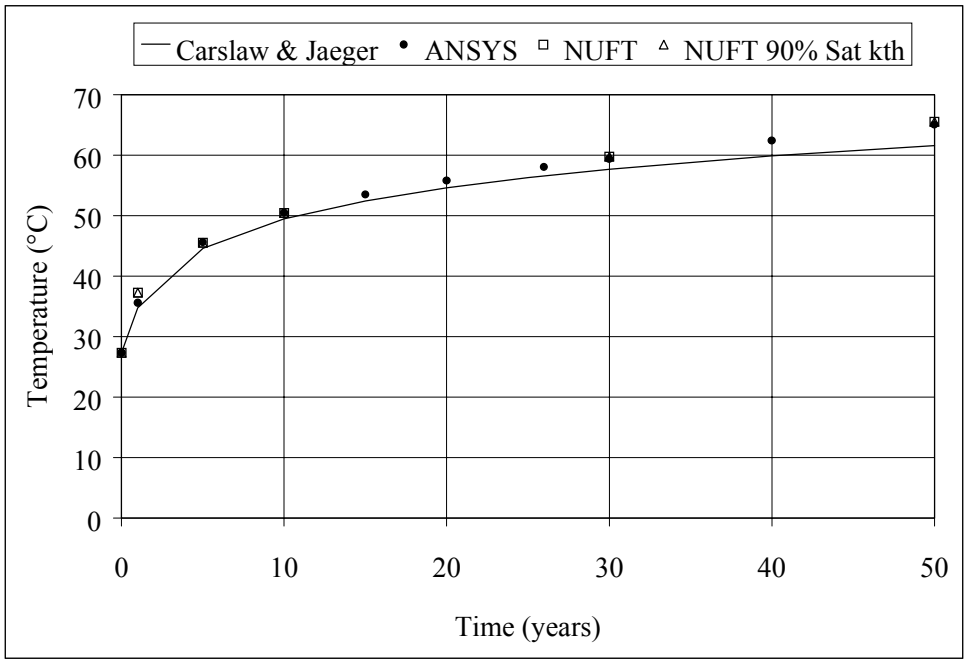

Figure 3. Rock Submodel Comparison using Conduction-Only Models. Divergence from the analytical solution with time is due the non-infinite domain of the numerical models.

Table 4 shows the results of simulations within the air sub-domain of the ventilation model. The differences in the waste package temperatures from the numerical models, compared to the analytic solutions, are small compared to the temperature rise from the air temperature or drift wall temperature (both 25°C [77°F] in these test problems). Each numerical model simulates the heat and/or mass transfer mechanism(s) being isolated, within a few degrees Celsius.

Table 4: Air Submodel Comparison

Method	T_{wp} at Steady State (°C)	$T_{model} - T_{analytical}$ (°C)
In-Drift Radiation Only Model (1 kW/m heat load, 0.847 effective emissivity)		
Analytical	58.8	N/A
ANSYS	57.7	-1.2
NUFT—stair-step drift	57.9	-0.9
MULTIFLUX	56.2	-2.6
In-Drift Convection Only Model (1 kW/ In-m heat load, 1.89 W/m^2 K convective heat transfer coefficient)		
Analytical	113.2	N/A
ANSYS	113.0	-0.2
NUFT—stair-step drift	115.9	2.7
NUFT—cylindrical	113.4	0.2
In-Drift Radiation and Convection Combined Model (1 kW/m heat load, 0.847 effective emissivity, 1.89 W/m^2 K convective heat transfer coefficient)		
Analytical	47.0	N/A
ANSYS	46.6	-0.4
NUFT—stair-step drift	50.1	3.1

Note: "Stair-step" refers to the use of rectangular grid elements to represent a curved surface. The alternative, "cylindrical" geometry uses curved surfaces, but cannot capture gravitationally driven processes when the cylinder axis is non-vertical.

3.3 COMPUTATIONAL FLUID DYNAMICS MODELING OF -NATURAL CONVECTION FOR 25-PERCENT- AND 44-PERCENT-SCALE TESTS AND AT REPOSITORY SCALE

The FLUENT (SNL 2001) computational fluid dynamics code has been used to model the potential repository, the 25-percent-scale ventilation test, and the natural convection test. For the 25-percent-scale ventilation test, there were two separate operating modes implemented. Most test runs used forced flow in which air was forced through the test section that includes heated cylinders representing the waste packages. A smaller number of runs used a natural convection mode, in which the ends of the test section were sealed off, eliminating forced flow and resulting in natural convection within the test section.

3.3.1 Ventilation Test Modeling

For the natural convection mode, FLUENT was used to predict the flow, temperature, and heat flux distributions in the test section. The details of the simulated waste package, which uses a small-diameter concentric heater rod in the waste package center, were included in the model since the heating of the waste package is nonaxisymmetric due to natural convection inside the simulated waste package. A two-dimensional model at the test center was developed to evaluate the natural convection within the waste package and within the test section. Buoyancy and radiation effects were included. The model used literature values or independent estimates of model parameters; and no adjustment of the model was made to enhance the data-model agreement.

The calculated temperature distributions in the natural convection mode of the ventilation test (without drip shield) are shown in Figure 4, indicating typical natural circulation patterns within

the waste package and between the waste package and the simulated drift wall. The temperature stratification is caused by natural convection, mostly within the upper half of the waste package and the test section, which is in agreement with the experimental data. The predictions of FLUENT matched the experimental data within a few degrees centigrade, including the vertical temperature stratification.

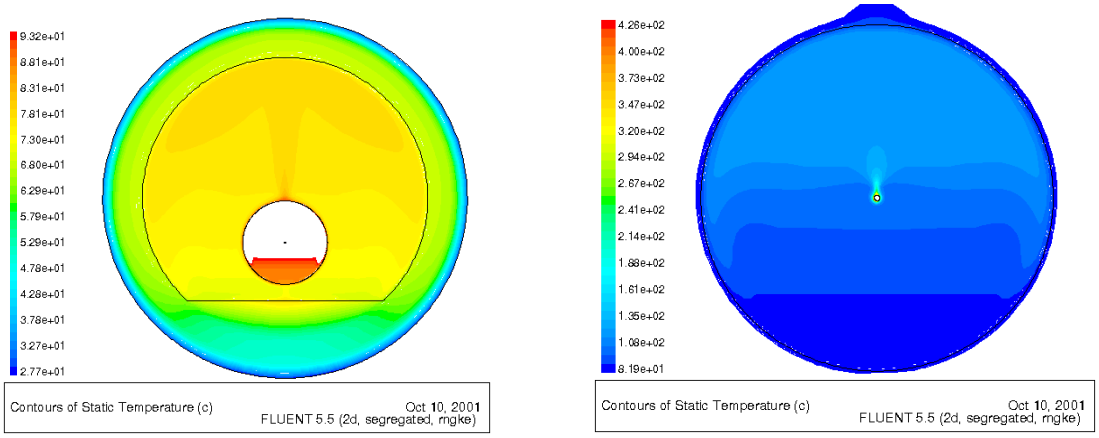

Figure 4. Calculated Temperature (°C) Distribution for the Natural Convection Mode of the 25-Percent-Scale Ventilation Test after Steady State is Achieved
The left graphic shows a cross section of the test section with no drip shield, including the waste package. The right graphic shows a cross section of the waste package interior.

3.3.2 Natural Convection Test Modeling

FLUENT has been used to perform three-dimensional pretest predictions for the 25-percent-scale natural convection test. The computational fluid dynamics calculations for various configurations have been completed—without a drip shield, with a continuous drip shield, and with individual drip shields over each waste package. As with the natural convection mode of the 25-percent-scale ventilation test, buoyancy effects and radiation are included.

For simplicity, a single waste package diameter was used in the pretest predictions. The calculated temperature distribution for a continuous drip shield is shown in Figure 5. The figure shows that the temperature plumes from the waste packages are essentially confined to underneath the drip shields, with some lateral spreading. For this heat load and an assumed ambient temperature of 27°C (81°F), the maximum waste package temperature in the test section is 41°C (106°F) after steady state is achieved.

Limited modeling of the potential repository has been done with the FLUENT computational fluid dynamics code. The preliminary calculations have been done at repository scale to check the performance of FLUENT and to compare the results to existing correlations and experimental data for natural convection in a horizontal concentric annulus.

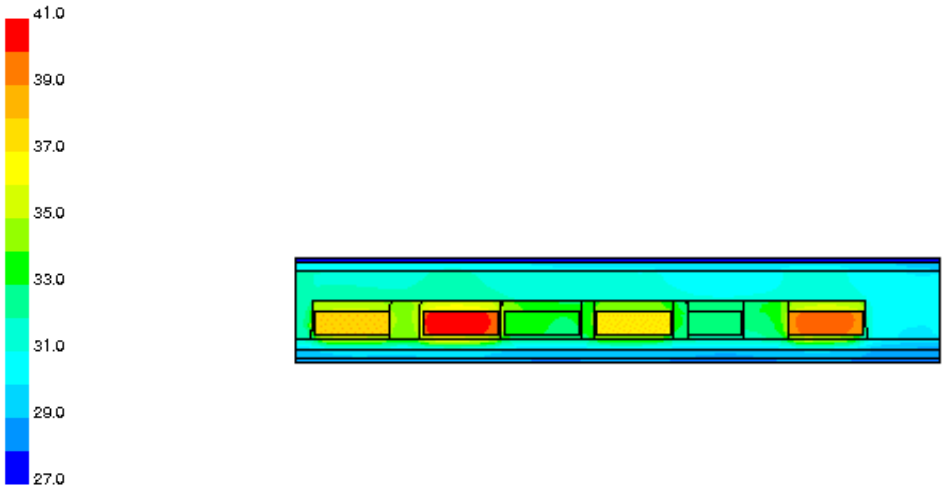

Figure 5. Side view of the Temperatures (°C) in the Natural Convection Test with a Continuous Drip Shield Installed, after Steady State is Achieved

3.3.3 Repository Modeling with Computational Fluid Dynamics Computer Codes

Calculations have been performed for the average equivalent (air) thermal conductivity predictions for a horizontal concentric cylinder as a function of Rayleigh number. The equivalent thermal conductivity is the ratio of heat transfer by natural convection and conduction to that for conduction alone. The solid and dashed lines in Figure 6 are the correlations of Kuehn and Goldstein (1976; 1978). These correlations are widely accepted as the best available predictive relationships for heat transfer in horizontal concentric cylinders. The correlations from these two papers are slightly different; the 1976 version is for any Prandtl number fluid, while the 1978 version is specific to air. The results from FLUENT for a concentric cylinder at the full repository scale are compared to the Kuehn and Goldstein correlations in Figure 6a. The computational fluid dynamics predictions are lower than the correlations by up to 35 percent at the higher Rayleigh numbers. In Figure 6b, experimental data for similar diameter ratios (Lis 1966; Kuehn and Goldstein 1978; Bishop 1988) have been added. Comparison to the data indicates that the Kuehn and Goldstein correlations overpredict that equivalent thermal conductivity at the higher Rayleigh numbers and that the FLUENT predictions are in better agreement with the experimental data.

3.4 RESULTS OF 25-PERCENT-SCALE FORCED VENTILATION TESTS

A four-phase 25-percent-scale ventilation test is being performed by the Yucca Mountain Site Characterization Project at the DOE Atlas Complex in North Las Vegas. The tests are designed to provide data to verify the ventilation model used for design and performance assessment. The first two phases of the test, which are completed, are:

- Phase 1—Heat-only test using ambient air ventilation
- Phase 2—Heat-only test using conditioned air (heated or cooled) for ventilation

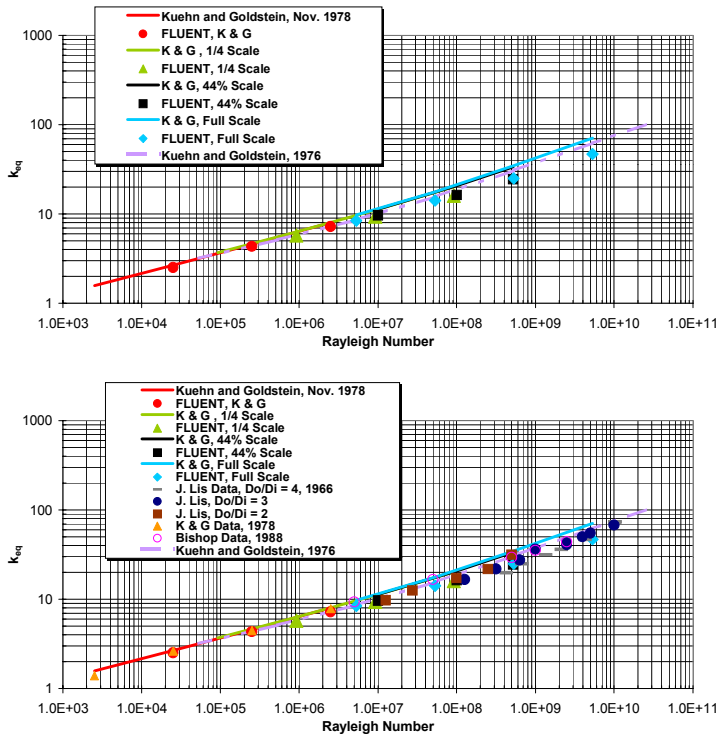

Figure 6. Comparison of FLUENT Results with Kuehn and Goldstein Correlations. The top graphic (a) compares the FLUENT results with the correlations. The lower graphic (b) compares both the FLUENT results and the correlations with experimental data.

Table 5 shows the results of several runs from these phases and how the inputs to the test are expected to scale to a repository. The first result in the table was reported in the *FY01 Supplemental Science and Performance Analyses* (BSC 2001a), Section 5.3.2.4.1. The other results have not been previously reported.

Table 5. Results from the 25-Percent-Scale Ventilation Tests

Power, kW/m		Flow Rate, m^3/s		Inlet Temperature (ºC)	Ventilation Efficiency for the Test
Repository Design	Test	Repository Design[a]	Test		
1.44	0.36	15	1	25	83%
1.44	0.36	15	1	45	70%
0.88	0.22	7.5	0.5	25	78%
0.88	0.22	7.5	0.5	35	69%

[a] Scaling based on equal air velocity

3.5 VALIDATION OF THE MULTISCALE THERMAL-HYDROLOGIC MODEL AND CORRECTIONS TO SUPPLEMENTAL TSPA MODEL RESULTS

The multiscale thermal-hydrologic model (MSTHM) was used to support the supplemental TSPA performed in the *FY01 Supplemental Science and Performance Analyses* (BSC 2001a). The MSTHM consists of four submodel types, which are run using the NUFT computer code (Nitao 1998). The results of the submodels are integrated with the multiscale thermal-hydrologic

abstraction code (MSTHAC). The MSTHM calculates the following thermal-hydrologic (TH) variables: temperature, relative humidity, liquid-phase saturation, liquid-phase flux, gas-phase composition, gas pressure, capillary pressure, water vapor flux, air flux, and evaporation rate. These variables are determined in or near the emplacement drifts throughout the repository footprint for a representative range of waste-package types.

Following the completion of the MSTHM calculations for the supplemental TSPA model, a model-validation effort was conducted (Buscheck et al. [in preparation]) for the MSTHM methodology implemented in MSTHAC, as well as for the NUFT submodels used in the supplemental TSPA calculations. This model-validation effort resulted in three findings (which are discussed in more detail in the remainder of this section of the white paper). First, MSTHM results were compared with a nested TH model, using the qualified NUFT code. The nested model includes a drift-scale mesh embedded within a mountain scale mesh for a single monolithic model of a small repository surrounded by unheated rock. The comparison included an improvement in the manner in which relative humidity is calculated on the drip shield in the MSTHM. Second, the thermal-radiation coefficients used in the two-dimensional line-averaged-heat-source, drift-scale thermal-hydrologic (LDTH) submodels had been underestimated using the RADPRO preprocessor during supplemental TSPA model calculations. The use of underestimated thermal-radiation coefficients in the cavity between the drip shield and drift wall results in reduced heat transfer between these surfaces and higher calculated waste package temperatures. Third, it was found that the manner in which temperature and relative humidity are averaged around the perimeter of the emplacement drift was not internally consistent in the supplemental TSPA model calculations. This resulted in supplemental TSPA model overprediction of relative humidity values during the boiling period, and underprediction in sub-boiling periods. The improvement in calculating relative humidity, made in MSTHAC during the model validation calculations, eliminates the inconsistency in the earlier supplemental TSPA model calculations.

3.5.1 Validation of the Multiscale Thermal-Hydrologic Model

The test problem used to validate the MSTHM represents a scaled-down repository, consisting of three 243-m (797-ft) long drifts embedded in a larger unheated rock domain. The thermal-operating parameters are equivalent to those of the supplemental TSPA model higher-temperature operating mode (HTOM). Four different kinds of waste packages are represented in the test case. These are an average 21-PWR assembly, commercial spent nuclear fuel waste package; a long high-level waste package; a design-basis 21-PWR waste package; and an average 44-BWR assembly waste package. The scaled-down repository was chosen as a model-validation test problem because it is not currently feasible to model the full repository system with a nested TH model.

For the test problem, both the MSTHM and the corresponding nested TH model discretely represented four individual waste packages. Each waste package and associated drip shield segment was treated as a monolithic heat source in both the MSTHM and nested TH model. This simplification was made to reduce the computational expense of representing waste packages in the nested TH model. These four waste packages were located at the center of the model repository (in Drift #2). The remainder of Drift #2, beyond the discretely represented waste-package locations, was a line-averaged heat source within the drip-shield monolith. For

Drifts #1 and #3, the heat-source representation was a line-averaged heat source distributed over the entire 5.5-m (18-ft) diameter cross section of the drift.

The nested TH model fully represents the three-dimensional model domain using a four-level nested numerical mesh, with the finest mesh surrounding the four discretely represented waste packages and the coarsest mesh in the far-field region away from the heated drifts. Both the MSTHM and the nested TH model utilize the stratigraphy and boundary conditions, including infiltration flux, appropriate for the geographic center of a full repository. The infiltration rates at this location are 5.7 mm/yr (0.2 in./yr) for the present-day climate (0 to 600 yr), 15.1 mm/yr (0.59 in./yr) for the monsoonal climate (600 to 2000 yr), and 23.2 mm/yr (0.91 in./yr) for the glacial-transition climate beyond 2000 yr.

Comparison of the predictions of temperature, relative humidity, and liquid-phase saturation at the drift wall, drip shield, and invert all show the MSTHM and the nested TH model to be consistent. Figure 7, which includes the correction and improvement to the MSTHM developed during the validation, compares the temperature and relative humidity at the drift wall and drip shield for an average 21-PWR commercial spent nuclear fuel waste package. The model-validation exercise demonstrates the validity of the fundamental approach that the MSTHM uses to modify two-dimensional LDTH submodel results with those of three-dimensional mountain- and drift-scale conduction-only thermal models to predict TH conditions in the Yucca Mountain repository system. The differences in the predicted TH behavior between the MSTHM and the nested TH model are small. Moreover, these small differences are negligible relative to the influence of parameter variability and uncertainty on predicted TH behavior.

3.5.2 Corrections and Improvements Made to MSTHM Calculations Supporting the Supplemental TSPA Model

As discussed above, the model-validation effort led to an improvement in how MSTHAC calculates relative humidity and to a correction to the thermal-radiation coefficients used in the LDTH submodels.

Relative Humidity Calculation—Output for the MSTHM calculations of the supplemental TSPA model were conducted using MSTHAC Versions 6.4.1 and 6.4.2. These versions of MSTHAC calculate the drift-wall temperature (for a particular geographic location in the repository and particular waste-package type) by averaging over the host-rock blocks at the perimeter of the excavated drift (including the blocks under the invert). However, the drift-wall relative humidity was calculated by averaging the values of the host-rock blocks at the crown and the bottom of the drift. This led to an overestimate of the drift-wall relative humidity during the boiling period. Because the drip-shield and waste-package relative humidity are related to the drift-wall relative humidity in the MSTHM, the relative humidity at the drip shield and waste package were also slightly overpredicted in the supplemental TSPA model, during the boiling period.

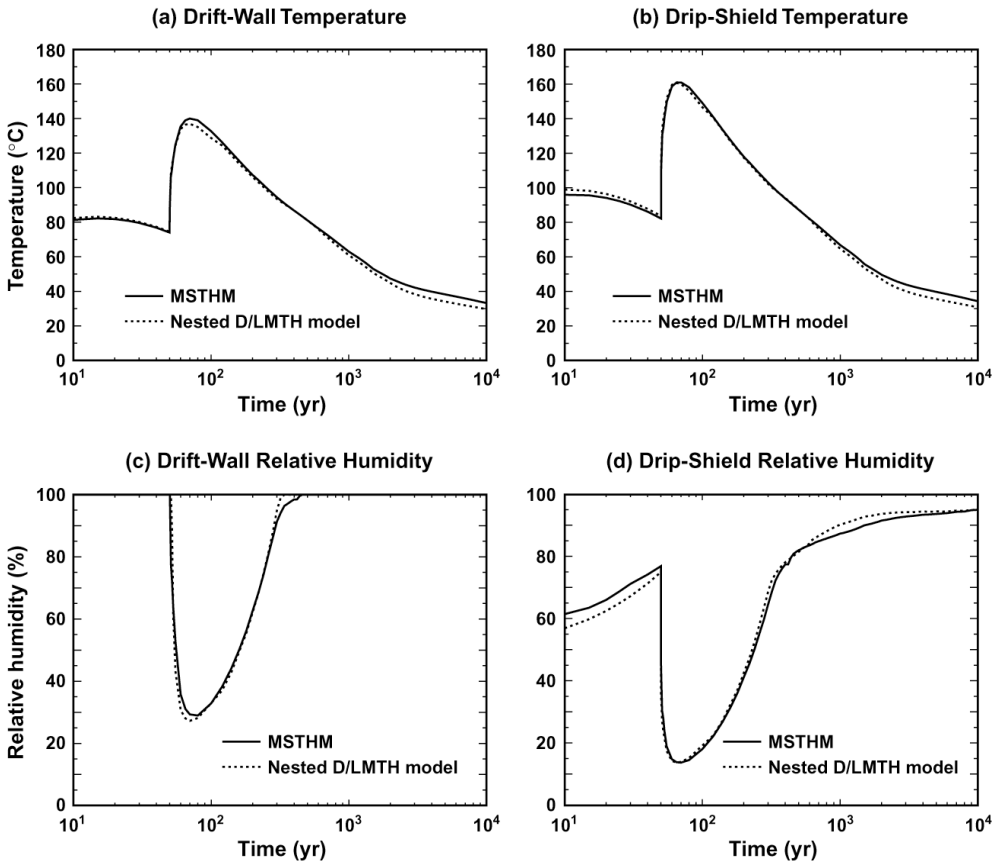

NOTES: The acronym D/LMTH model indicates discrete/line averaged-heat-source, mountain-scale thermal-hydrologic model. The change in thermal performance at the cessation of ventilation at 50 years is clear in each panel.

Figure 7. Temperature and Relative Humidity at the Drift Wall and on the Drip Shield vs. Time for the MSTHM and the Nested D/LMTH Model for an Average 21-PWR Commercial Spent Nuclear Fuel Waste Package

It was found that to calculate the drip-shield relative humidity, both the drift-wall relative humidity and temperature should be perimeter-averaged around the air-filled cavity in the drift. These averages should include the porous media interfaces to the air, i.e., the drift wall above the invert and the top of the invert outside of the drip shield. However, relative humidity in the host rock immediately below the invert should not be included in this perimeter average.

Thermal Radiation Coefficients for the LDTH Submodels—For the supplemental TSPA model, the thermal radiation coefficients for the cavities inside the two-dimensional LDTH and three-dimensional discrete-heat-source, drift-scale thermal (DDT) submodels were generated using RADPRO Version 3.22 software, which is qualified to generate three-dimensional thermal-radiation coefficients for three-dimensional models. Subsequent to submitting the supplemental TSPA model MSTHM calculations, an analysis was conducted to investigate the validity of applying the three-dimensional thermal-radiation generation feature in RADPRO v3.22 to two-dimensional models. It was found that, for the three-dimensional RADPRO calculation to produce applicable two-dimensional LDTH radiation view factors, the representation had to be sufficiently long (> ~20 m (66 ft), or ~10 times the radial gap between

components) in the third dimension (i.e., along the drift axis). Because the supplemental TSPA model RADPRO calculations for the two-dimensional LDTH submodel were shorter than this 20-m (66-ft) requirement, the thermal-radiation coefficients were underestimated.

The use of underestimated thermal-radiation coefficients in the cavity between the drip shield and drift wall resulted in decreased heat transfer between these surfaces. The decreased heat transfer caused the calculated temperature difference between the drip shield and drift wall to be too large, which resulted in the peak drip-shield and waste-package temperatures being as much as ~6°C (11°F) overpredicted for the HTOM and as much as ~2°C (4°F) overpredicted for the LTOM (Figure 8). After the temperature peaks, the magnitude of the overprediction diminishes quickly with time. Because of the overprediction of the temperature difference between the drip shield and drift wall, the reduction in relative humidity between the drip shield and drift wall was also overpredicted (by a few percent).

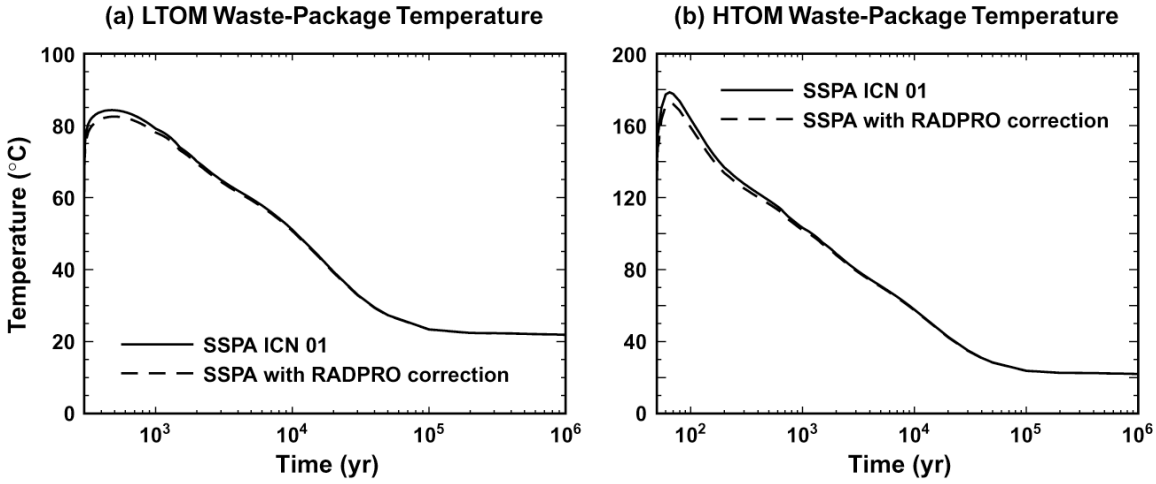

Figure 8. Temperature Calculated by the MSTHM for a Design-Basis 21-PWR Commercial Spent Nuclear Fuel Waste Package, for the Supplemental TSPA Model and after Correction of RADPRO-Calculated Thermal Radiation Coefficients in the NUFT LDTH Submodels.

Thermal-radiation coefficients in the three-dimensional DDT submodels were correctly generated by RADPRO v3.22; therefore, the temperature and relative humidity differences between the waste package and drip shield were correctly predicted, as was the waste-package-to-waste-package variability of temperature and relative humidity.

3.5.2 Comparison of MSTHM Calculations Supporting the Supplemental TSPA Model

Figures 8 and 9 show temperature and relative humidity for a design-basis 21-PWR waste package predicted by the MSTHM at the center of the repository for the supplemental TSPA model, the corrected RADPRO-calculated thermal-radiation coefficients in the LDTH submodels, and the improved representation of relative humidity in MSTHAC. The RADPRO correction affects both temperature and relative humidity, and the relative humidity calculational

improvement affects only relative humidity. Relative to the supplemental TSPA model case, the changes to the MSTHM result in the following observations:

- The improved relative humidity representation in MSTHAC has no influence on temperature for either the LTOM or HTOM.
- The improved relative humidity representation in MSTHAC results in a small increase in relative humidity for the LTOM.
- The improved relative humidity representation in MSTHAC results in a small decrease in relative humidity for the HTOM during the boiling period and a small increase in relative humidity during the post-boiling period.
- The correction to the RADPRO-calculated thermal-radiation coefficients in the LDTH submodels causes a small decrease in waste package temperature, with the maximum decrease occurring when temperature peaks. The decrease in the peak temperature is 1.7°C (3°F) for the LTOM and 6°C (11°F) for the HTOM.
- The correction to the RADPRO-calculated thermal-radiation coefficients in the LDTH submodels, together with the improved relative humidity representation in MSTHAC, causes a small increase in relative humidity for the LTOM.
- The correction to the RADPRO-calculated thermal-radiation coefficients in the LDTH submodels, together with the improved relative humidity representation in MSTHAC, has little effect on relative humidity during the boiling period, and causes a small increase in relative humidity for the HTOM during the post-boiling period.

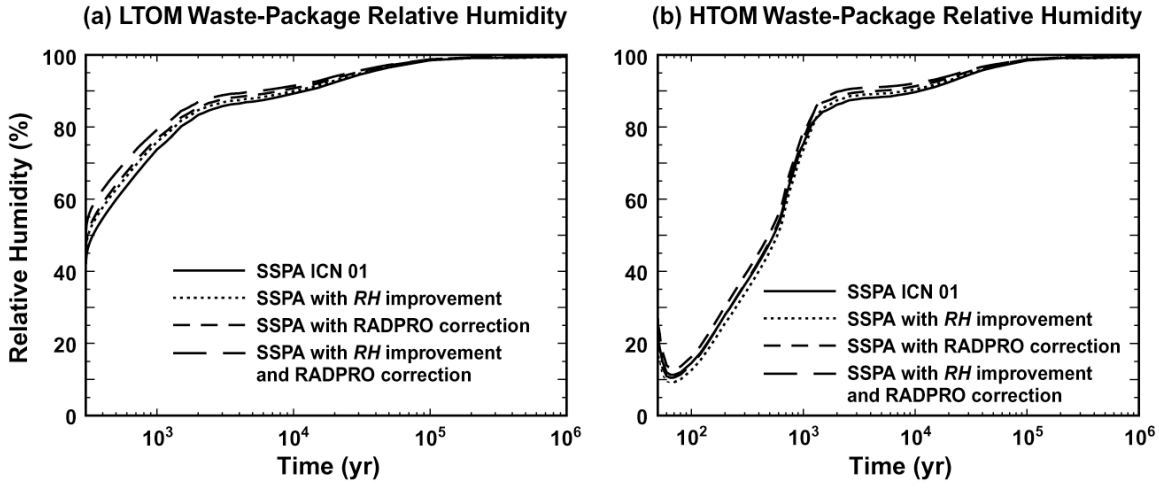

Figure 9. Relative Humidity Calculated by the MSTHM for a Design-Basis 21-PWR Commercial Spent Nuclear Fuel Waste Package, for the Supplemental TSPA Model, after Correction in RADPRO-Calculated Thermal-Radiation Coefficients in the NUFT LDTH Submodels, and after Improving the Representation of Relative Humidity in MSTHAC

3.6 THERMAL CONDUCTIVITY MODELING AND DATA AT LABORATORY AND FIELD SCALES

Thermal analyses for the repository horizon in the supplemental TSPA model were developed using thermal conductivity estimates based on temperature data collected from several thermal field tests and laboratory measurements of thermal conductivity. Both the field tests and the majority of the laboratory samples were in the Topopah Spring nonlithophysal unit. The majority of the repository emplacement drifts, however, will be located in the Topopah Spring lower lithophysal unit (Tptpll). At the time of *FY01 Supplemental Science and Performance Analyses* (BSC 2001a) preparation, no field tests had been conducted in the lower lithophysal unit where convection, vapor transport, and the presence of lithophysal voids could significantly influence thermal transport phenomena. A small number of core samples have been tested from the Tptpll matrix; however, the core is smaller than many lithophysae, so that these measurements did not fully address drift- and repository-scale heat transfer.

The overriding characteristic of the Tptpll stratigraphic unit consists of lithophysae (voids) of sizes ranging from less than a centimeter to over 1 meter in diameter. These voids will decrease rock mass thermal conductivity in comparison to nonlithophysal rock. The rock mass also contains a pervasive fracture network that locally interconnects the lithophysae.

The field thermal conductivity test program was started in the ECRB Cross-Drift in March 2001. One test has been completed in the Tptpll unit. The first stage of the test was conducted at low heater power, and measurements are made below boiling, at in situ moisture conditions. During the second stage, the heater power was increased until a dryout zone was created, at which time thermal property measurements were repeated.

The test is located at Station 15+66.07 m of the ECRB. The layout of that test, shown in Figure 10, consists of a 5-m (16-ft)-long, 5 kW, rod heater in a 7.6-cm (3-in.) diameter horizontal borehole angled at 45° to the drift wall. Temperatures were measured at 30 positions along 5 m (16 ft) of a second borehole that crossed the heater borehole oriented perpendicular to the heater. The instrument borehole was 16-cm (6.3-in.) center to center above the heater borehole (8.4 cm (3.3 in.) of rock between the hole edges).

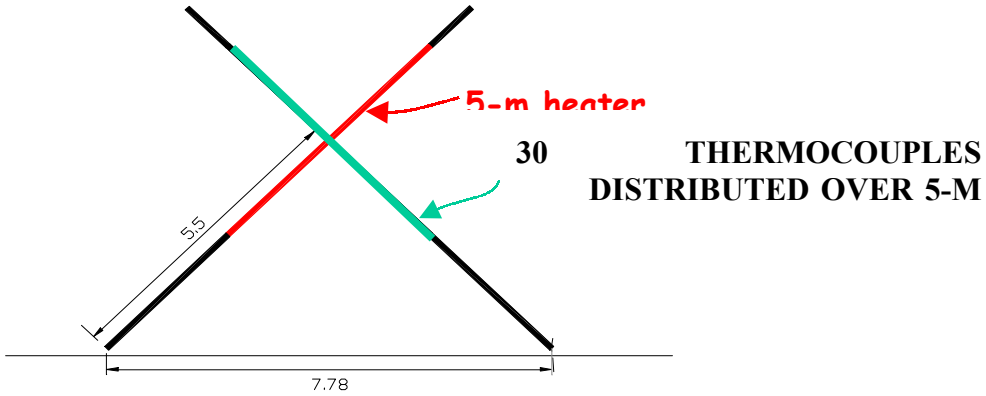

Figure 10. Geometric Layout of the First Thermal Conductivity Field Test

The first stage of this initial in situ thermal conductivity field test has been completed. The heater was run at approximately 433 W for almost 30 days. The temperatures, measured at different times, are shown in Figure 11. Data from one thermocouple were not used due to a suspected mechanical failure for that sensor. A second, temporary, operational problem at the start of the test resulted in loss of all sensor data between approximately 0.2 and 2.7 days. The initial saturation during the temperature measurements is being inferred from pretest neutron logging of the borehole and measurements on core samples. The neutron log data display a near-constant value from 3 m (10 ft) to the 8-m (26-ft) depth of the hole. Previous measurements suggest that this value would be similar to the far-field value, which is somewhat greater than ~80 percent saturation.

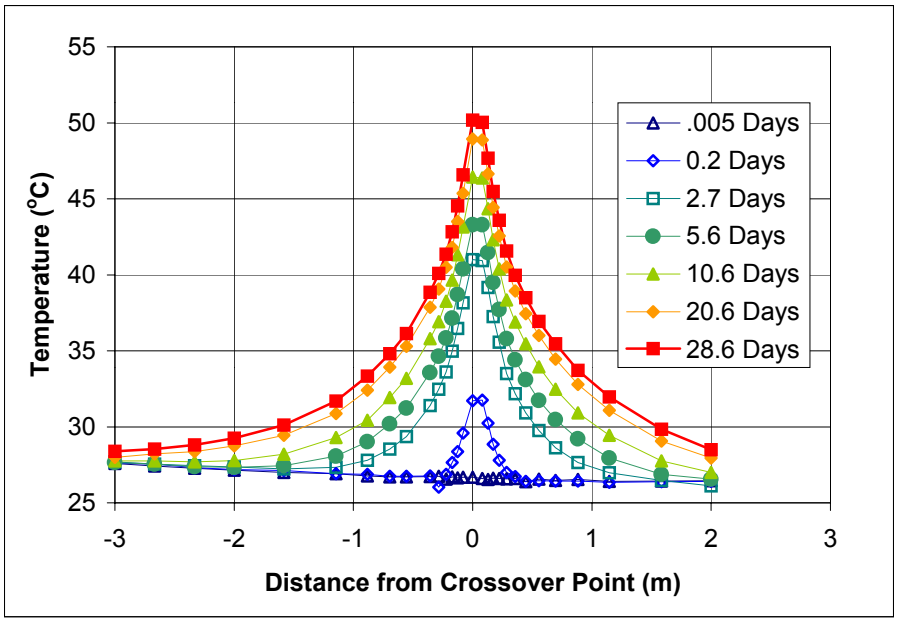

Figure 11. Temperatures Measured at Selected Times as a Function of Distance from the Point at which the Instrumentation Borehole Crosses over the Heater

These data were analyzed using a solution from Carslaw and Jaeger (1959). The temperature at a point any distance from a heated sphere in an isotropic homogeneous medium is calculated using the following equation:

$$T = \frac{a^2 F_0}{Kr}\left\{ erfc\,\frac{r-a}{2(kt)^{1/2}} - \exp\left[\frac{r-a}{a} + \frac{kt}{a^2}\right] erfc\left[\frac{r-a}{2(kt)^{1/2}} + \frac{(kt)^{1/2}}{a}\right]\right\} \qquad (1)$$

where:

T = Temperature (K)
a = Radius of sphere (m)
F_0 = Heat flux at surface of sphere (W/m^2)
K = Thermal conductivity (W/m•K)
r = Distance from center of heater to measurement point (m)
k = Thermal diffusivity (m^2/s)
t = Time (s)

The temperatures around a finite length line source heater are predicted by approximating the heater as a series of 1,312 small overlapping spheres, each with a diameter equal to the borehole diameter. The predicted temperature at each thermocouple location is calculated by summing the contributions from each sphere. The values of thermal conductivity and thermal diffusivity are obtained by comparing measured temperatures with those predicted using Equation 1, using initial-guess values of thermal conductivity and diffusivity. The error is taken as the sum of the squares of the differences between measured and predicted values. The Mathcad standard 'Minerr' function is used to minimize this error by adjusting the values of thermal conductivity and thermal diffusivity.

Reduced data are shown in Figure 12. At a given time, thermal conductivity and thermal diffusivity are calculated using the difference between temperature at that time, and temperature as measured before initiation of heating. At greater times, a larger rock volume participates in the test. The scatter at the very beginning of the test may be due to the heating up of the heater assembly itself. The data used in the analysis were taken at 0.1, 0.2, 2.7, 3.0, 3.6, 4.6, 5.6, … 28.6 days. The number of data times (30) used in the data reduction was selected to be similar to the number of spatial locations (29). To minimize the influence of human activity in the facility, a data point recorded near midnight was used, except at early times when more frequent data sampling was used. When the early-scatter data at 0.1 and 0.2 days are omitted, values of 1.74 W/m•K and 8.2×10^{-7} m^2/s are obtained for thermal conductivity and thermal diffusivity, respectively.

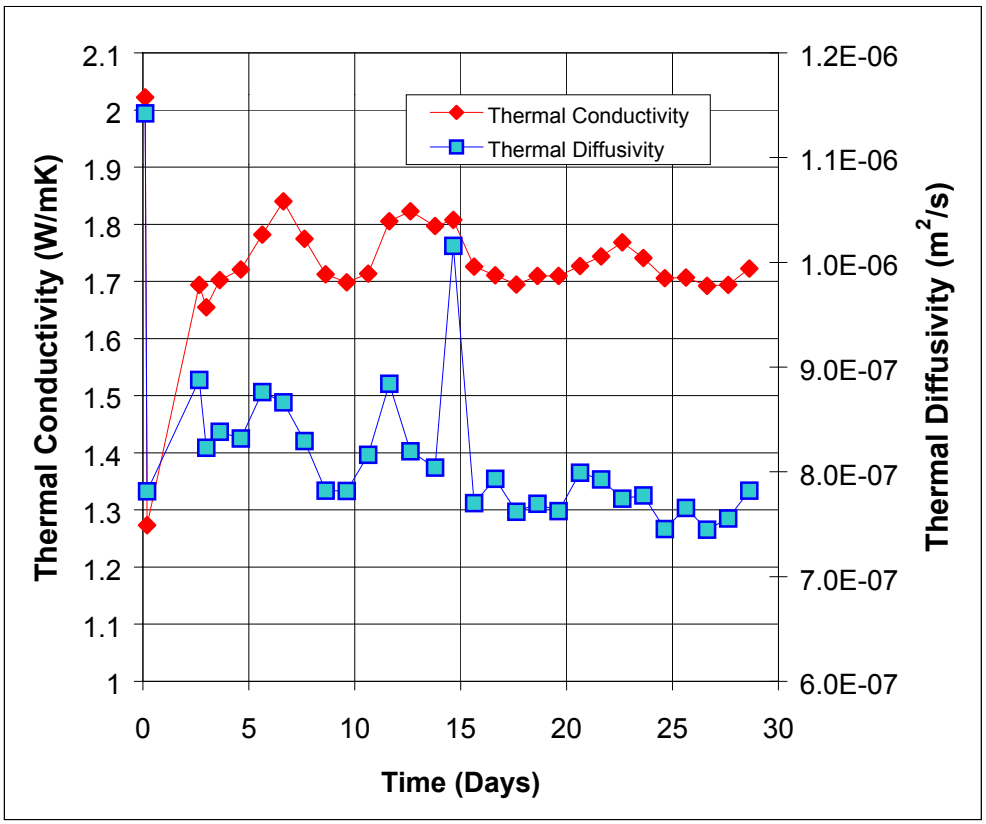

Figure 12. Values of Thermal Conductivity and Thermal Diffusivity Calculated from the First In Situ Field Test

3.7 MODELING OF CONDENSATION ON EBS SURFACES

Condensation under the drip shield is coupled to other physical processes (Figure 13, which shows a longitudinal cross section of a drift). Evaporation immediately below the hotter waste packages absorbs heat and decreases the local net heat flux entering the invert. Condensation immediately below the cooler waste packages releases heat and increases the local net heat flux entering the invert. The temperature range among the components within the drift will be smaller due to the heat flux leveling effect of evaporation and conduction. The net effect will be the same as if the thermal conductivity of the air under the drip shield were substantially increased for some thermal flux paths.

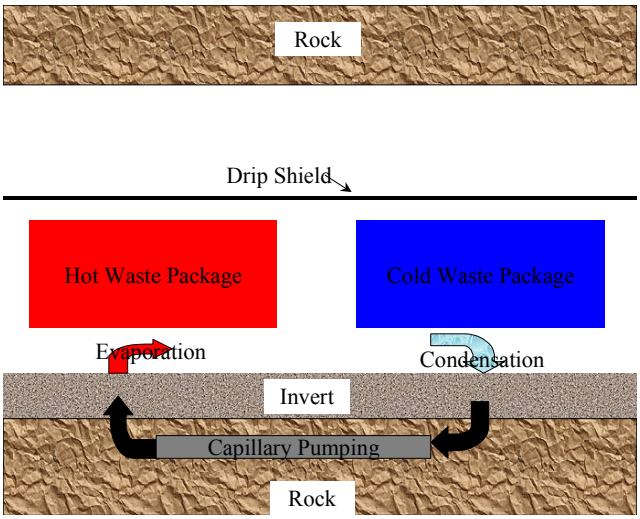

Figure 13. Temperature Effects of Evaporation and Condensation

Quantification of this condensation/evaporation process is inhibited by numerical limitations. Most of the coupled TH models currently in use are two-dimensional. The three-dimensional TH models needed to directly solve this problem take too long to run for routine use. For this reason, an energy bound approach is being used to address the potential condensation rate.

There are three energy bounds that can be constructed. The simplest is that the condensation rate cannot exceed the power produced by the waste packages divided by the latent heat of water. This is an absolute bound, but the bound is quite high for early times.

The second bound assumes that the condensation rate cannot exceed the power entering the invert under the drip shield, divided by the latent heat of water (i.e., it assumes that most in-drift condensation originates from in-drift evaporation from the invert). The power entering this portion of the invert is approximated using the three-dimensional DDT submodel of the multiscale thermal-hydrologic model. This submodel calculates conduction and radiation explicitly, and approximates convection using an enhanced thermal conductivity approach. Because the dominant heat transfer mode under the drip shield is radiation, the DDT submodel should produce a reasonable estimate of energy partitioning throughout the drift. This bound assumes that there is only slow air exchange between the region under the continuous drip shield and the region above the drip shield.

The third energy bound is based upon the observation that the evaporation/condensation process would drive the domain under the drip shield toward a more uniform temperature. The bounding analysis assumes that the rate of evaporation is the limiting factor and that capillary pumping, convective transport, or condensation nucleation do not slow the rate. This asymptotic limit was simulated in the DDT submodel by replacing the waste packages and air under the drip shield with a composite material having the same total heat capacitance and a very high thermal conductivity. The two sets of invert heat fluxes were then compared on a cell-by-cell basis. The invert cells in which the more-nearly-isothermal condition has decreased the surface heat flux would be associated with evaporation in a realistic three-dimensional heat and mass transfer calculation. The invert cells in which the more-nearly-isothermal condition has increased the surface heat flux are associated with condensation. The maximum rate of evaporation (and hence condensation) under the drip shield is determined by dividing the total change in heat flux associated with evaporation by the latent heat of water.

Results of the 46 MTU/acre thermal analysis are shown in Figure 14. In the absence of evaporation, the power entering the invert (dotted blue line) is about one-tenth the total power (solid red line). In the presence of evaporation (the third bounding approach), the power entering the invert is reduced (dashed green line). The maximum evaporative power, based upon the third limit (black dot-dash line), is approximately 1.5 to 3 percent of the total power.

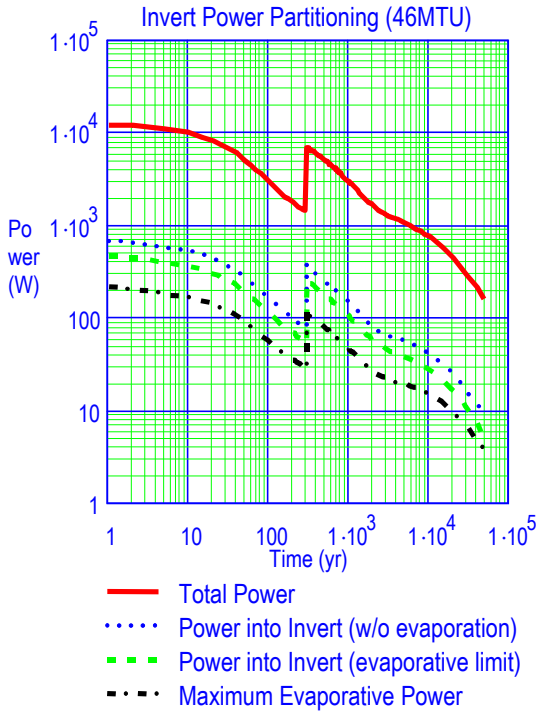

Figure 14. Estimation of the Invert Evaporation Rate Using the Third Bounding Approach

The evaporative limit (third bound) is shown in Figure 15 as an equivalent superficial velocity flowing into the invert (liquid flux divided by the invert area under the drip shield). The liquid flux was inferred from the heat flux as described above. The liquid flux is evaporated in warmer axial locations of the invert, and condenses in cooler locations (on or above) the invert. The

bound decays from a peak of about 13 mm/yr (0.5 in./yr) at the time of drift closure to about 1 mm/yr (0.04 in./yr) at about 50,000 years. For comparison, the ambient percolation rate in the host rock ranges from a less than 1 mm/yr (0.04 in./yr) to over 100 mm/yr (4 in./yr), depending on the climate state and the location in the potential repository footprint.

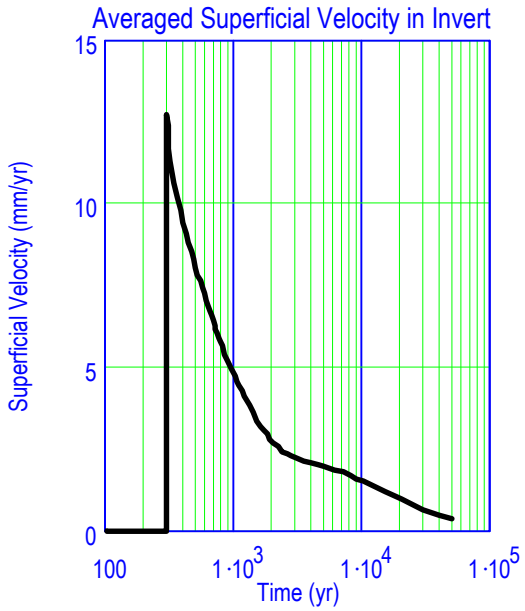

Figure 15. Invert Effective Flux Limit, Based on the Third Evaporation Bound

A number of factors serve to make this an upper bound of condensation at any location under the drip shield. First, phenomena such as capillary pumping in the rock and invert, thermal and diffusive boundary layers, and convective mass transport in the gas have all been replaced with the asymptotic limit of a high conductivity region under the drip shield. Each of these processes serves to retard the evaporation/condensation process.

Second, the DDT conduction/radiation submodel was used to compute the heat fluxes into the invert for the evaporative limit (third bound). Had a full TH calculation been performed, evaporation and condensation in the invert would have decreased the temperature differences between packages. The result would have been a smaller difference in heat fluxes in the invert and, consequently, a smaller bound on the condensation rate.

Finally, this bounding calculation ignores the transfer of gases between the region under the drip shield and that outside the drip shield. The air outside the drip shield is cooler than any surface under the drip shield. Hence, it is unlike that any air exchange across the drip shield would increase the condensation under the drip shield. However, such air exchange could result in increased evaporation under the drip shield and condensation outside the drip shield, increasing the temperature leveling effect of evaporation and condensation within the engineered barrier system.

A number of caveats accompany this analysis. Condensation under the drip shield is dependent upon the specifics of the drip shield design. This analysis presumes that the drip shield is a

continuous structure that extends the entire length of the tunnel. If, instead, the drip shield were composed of multiple units of finite length, convective flows might be sufficient to reduce the relative humidity in the vicinity of the drip shield surface. Condensation might take place at the drift walls rather than at the drip shield surface. If this were true, condensate would never be able to enter the waste package unless affected by deliquescence phenomena, in which chemical effects drive condensation onto dust, for example, at relative humidity less than 100 percent.

Condensation variability at a larger scale along the length of the drifts could also be a factor. The outer edges of the repository (at the eastern and western margins) will naturally cool faster than the center. Drifts that extend from the center of the repository to the outer edges will have axial temperature gradients that result from edge cooling (i.e., locations at the repository edges cool faster than those at the center, due to lateral conduction). The Drift Scale Test in the Exploratory Studies Facility has already demonstrated that a significant fraction of the water evaporated in the rock can escape through the leaky bulkhead to the access drift. In a sealed drift, water vapor would diffuse toward the cooler outer edges where it would condense. This process would serve to make the repository temperatures more uniform than currently predicted as well as increasing the local condensation rate for finite periods of time. Depending upon the drip shield design, a portion of this axially-dependent condensation could take place under the drip shield.

Finally, barometric pumping could influence condensation. The access drifts, even though they may be backfilled, will likely provide a high-permeability path from the surface to the emplacement drifts. The contrast between the permeabilities of the access drifts and the undisturbed rock cause a time shift in the propagation speed of the barometric pressure fluctuations. This causes the drift to exchange air with the voids in the surrounding rock. Since the surrounding rock is cooler than the air in the drift, this should result in a lower relative humidity in the emplacement drift than is currently predicted, which, in turn, would decrease or eliminate condensation under the drip shield. This situation is analogous to the Drift Scale Test in the Exploratory Studies Facility, in which the relative humidity behind the bulkhead fluctuates with the barometric pressure.

3.8 DUAL-PERMEABILITY MODELING OF THE INVERT

In previous analyses for TSPA-SR model and supplemental TSPA model, a single continuum approximation was used to represent hydrologic properties and performance of the invert ballast material. The invert ballast material is comprised of crushed tuff. Crushed tuff contains two types of porosity, an intra-granular matrix porosity component (within the grains) and an inter-granular pore space component (between the grains). Each of these porosity components has distinct intrinsic hydrologic properties. The single continuum approach does not explicitly represent the hydrologic properties for each porosity component but instead represents hydrologic behavior of the crushed tuff with a single set of average properties. An alternate conceptual model of invert hydrologic performance is being assessed with a dual-permeability model approach wherein each porosity component is represented explicitly. This approach allows the intra-granular and inter-granular porosities to behave in a manner consistent with their respective intrinsic hydrologic properties (e.g., capillary suction potentials).

A series of NUFT simulations have been performed to examine hydrologic performance of the invert using the van Genuchten model and different grain sizes, specific grain/void contact areas, host-rock properties, infiltration rates, and invert thickness values. The input parameters for the dual-permeability model and the results of the NUFT calculations are summarized below.

The NUFT simulations are based on the same inputs, assumptions, and qualified software (NUFT Version 3.0s [LLNL 1999] and XTOOL Version 10.1 [LLNL 2000]) used in *In-Drift Thermal-Hydrological-Chemical Model* (BSC 2001d). The key changes for the current calculations are the use of a dual-permeability model and better spatial resolution for EBS components:

- A dual-permeability model has been used for the geologic media surrounding the drift and for the invert ballast material (DTN: LB990861233129.001), rather than a single continuum model. It is appropriate to model the invert with the dual-permeability approach because the crushed tuff has an intra-granular matrix component and an inter-granular pore space component. The dual-permeability approach is consistent with the anticipated response of the tuff grains, where the matrix component will behave like the host rock and the large, inter-granular pore spaces will act as a capillary barrier to incoming flow from the host rock.

- The simulation grid (see Figure 16) is finer than that used in the in-drift thermal-hydrologic-chemical model to provide more spatial resolution in the invert and to provide better definition of the shapes of the waste package, drip shield, invert, and the air gap between waste package and invert.

The hydraulic response of the inter-granular pore space is represented as a relationship between matric potential and moisture content. This relationship is based on the van Genuchten model (Fetter 1993). Figure 17 presents the van Genuchten curve fit to moisture retention data. The van Genuchten relationship between unsaturated hydraulic conductivity and matric potential (Fetter 1993) is presented in Figure 18.

Table 6 summarizes the computational results at 10,000 years for grain sizes of 0.317-mm (0.012-in.) diameter and 3.0-mm (0.1-in.) diameter. The data in Table 6 demonstrate that:

- The saturation of the grains is equal to the saturation of the host rock. This is a reasonable response because the tight pores in the tuff grains have high capillarity that draws water from the fractures of the host rock into the grains.

- The saturation of the inter-granular pore spaces is zero, confirming that the pore space acts like a capillary barrier.

- The vertical pore velocity is low and decreases with increasing grain diameter. This is again reasonable because coarser grains should act as a stronger capillary barrier than finer grain sizes.

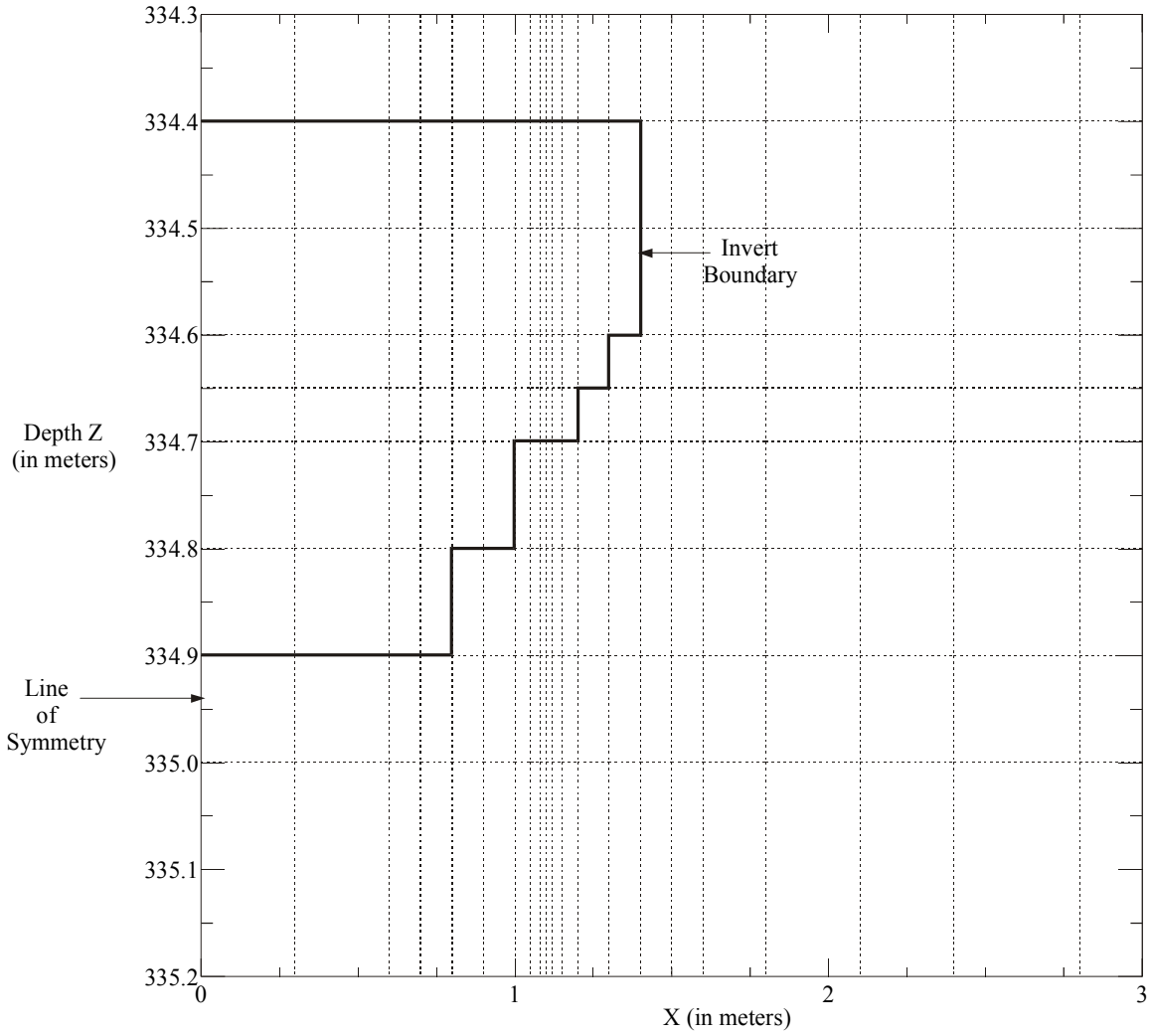

Figure 16. NUFT Simulation Grid

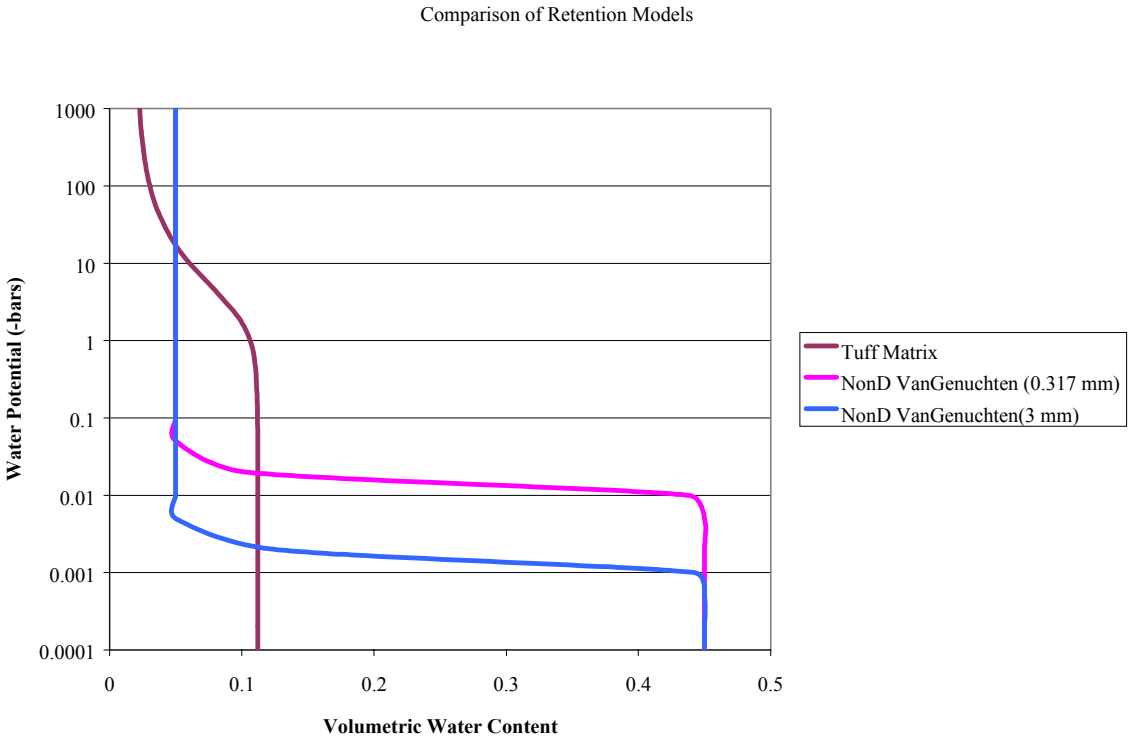

Figure 17. Water Retention Relationships for the Invert

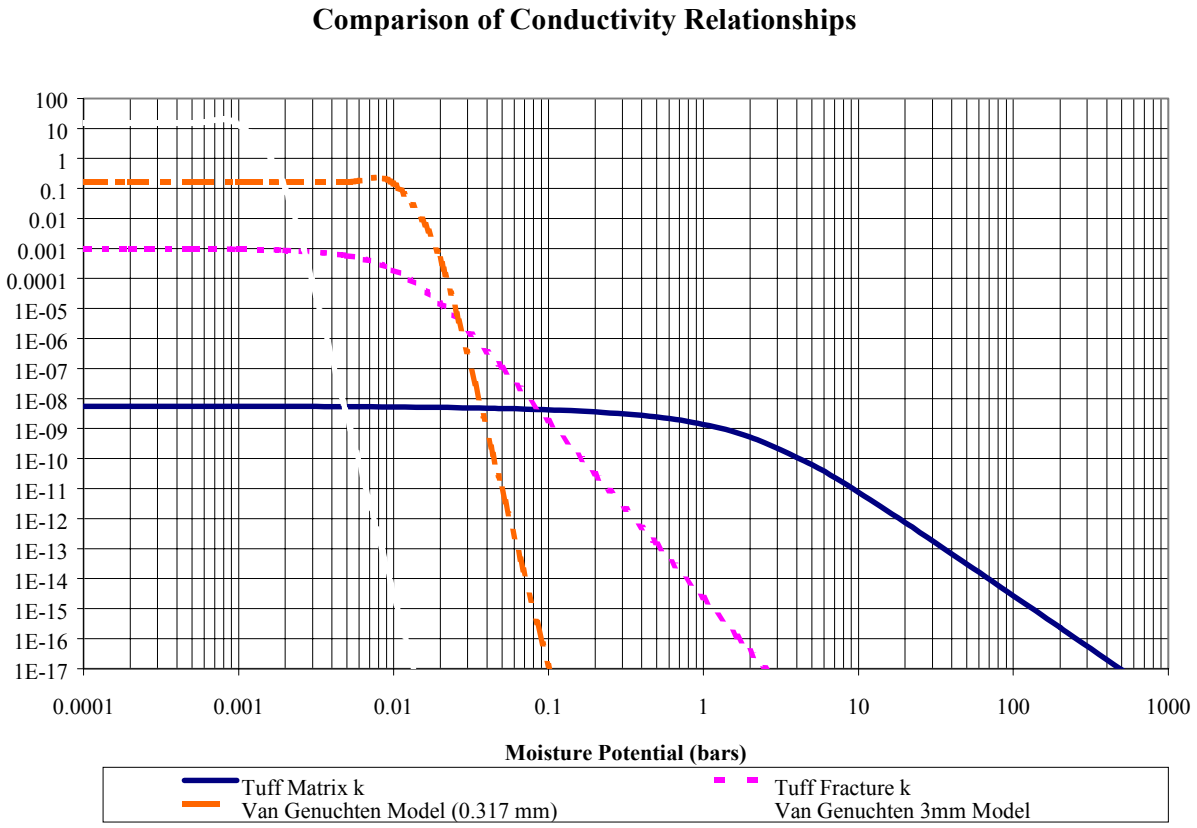

Figure 18. Relationship of Hydraulic Conductivity to Matric Potential for the Invert

Table 6. Comparison of Invert Conditions at Steady State (10,000 years) for the van Genuchten Model

Component/Parameter		Grain Diameter	
		0.317 mm	3.0 mm
Inter-granular Component	Porosity	0.450	0.450
	Saturation at Center of Invert	0.0	0.0
	Capillary Pressure (Pa) at center	3377	357
	Vertical Pore Velocity (m/s) along centerline	0.0	0.0
Intra-granular (Matrix) Component	Porosity	0.112	0.112
	Saturation at Center of Invert	0.999	0.998
	Capillary Pressure (Pa) at center	9368	14,100
	Vertical Pore Velocity (m/s) along centerline	7.6×10^{-11} to 1.8×10^{-10}	5.9×10^{-11} to 1.3×10^{-10}

3.9 INVERT DIFFUSION STUDY

The objective of the EBS in-drift diffusion study is to characterize and reduce uncertainties associated with measurement of the diffusion coefficient and modeling of diffusion processes in the invert. The results of this work will contribute to a detailed, process-level understanding of the diffusion of radionuclides through crushed tuff or another granular material in the invert.

Phase 1 of the study has been completed. The scope of this first phase included three tasks:

1. Review of the literature on diffusion data to determine if the functional dependence of diffusion coefficient on bulk moisture content, as used by TSPA-SR, properly represents the diffusive behavior of porous gravel

2. Evaluation/verification of the electrical conductivity/Nernst-Einstein method to infer values of the diffusion coefficient

3. Development of an alternate approach for direct measurement of the diffusion coefficient through microscale profiling of diffusing tracers.

The results for each task are summarized in this section. All tasks were conducted under applicable quality assurance requirements, and documented in Scientific Notebooks YMP-LBNL-JSW-QH-1E (pages 91 to 147), YMP-LBNL-JSW-QH-2 (pages 1 to 63), YMP-LBNL-JSW-TJK-1 (pages 1 to 97), and LLNL-SCI-4G2-VI (pages 1 to 18).

3.9.1 Literature Review

A thorough literature review has been conducted and the results have been submitted to a peer-reviewed journal (*Critical Reviews in Environmental Science and Technology*) for potential publication (Hu and Wang [in preparation]). This literature review focused on the behavior of, and relationship between, nonsorbing diffusion species and water content, particularly for porous aggregates (e.g., rock gravel). At low moisture contents, aqueous diffusion is postulated to occur in thin liquid films on the gravel surfaces, and the diffusion will be very slow if the water film is discontinuous. Diffusion is monotonically related to water content, but the relationship is complex and may vary with the range of water content (e.g., different relationships at different water-content ranges). The literature data further show that the relationship is related to the texture of the geologic medium. Figure 19 (from Hu and Wang [in preparation]) presents the relationship, based on data compiled from the literature, between diffusivity ratio (ratio of effective diffusion coefficient D_e to aqueous diffusion coefficient D_0) and the water content for media with different textures. The relationship appears to be related to potential energy status or mobility of water rather than just the magnitude of water content. The location of the curve is related to the texture, with coarse-textured media to the left and fine-textured media to the right.

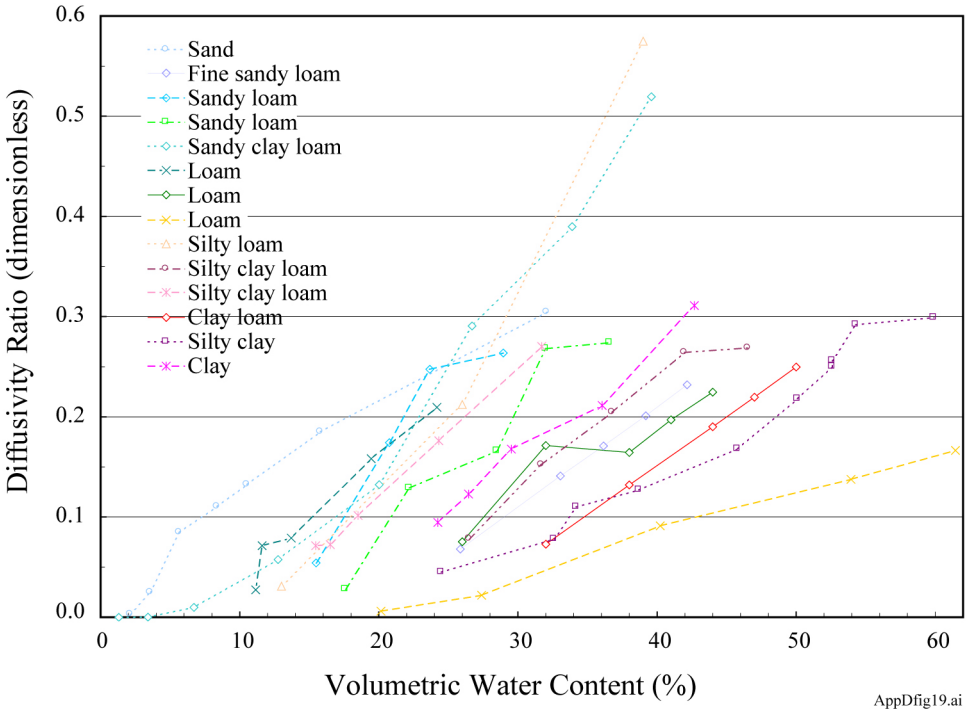

Figure 19. Compilation from the Literature on Diffusion Data as a Function of Water Content, Showing the Effect of Medium Texture on Diffusion and Critical Water Content (from Hu and Wang [in preparation])

Porous-rock gravel, such as crushed tuff, exhibits unique water distribution characteristics. Rock surfaces in partially saturated environments will generally be wetted by liquid films that can be held either by adsorptive forces on mineral surfaces or by capillary effects in surface roughness. For a porous-rock-gravel system, the total water content is comprised of surface water (including surface film water around grains and pendular water between rock grain contacts) and internal water (water contained within the rock matrix pores). This internal water is not likely to contribute significantly to water flow and transport in the unsaturated gravel system (Conca and Wright 1990). Pendular water elements between gravel grains serve as the bridging pathways between grains and control the efficiency of the system in attaining the upper limit of transport determined by surface films. Diffusion in rock gravel could be very slow because water films on surfaces can be discontinuous or absent.

3.9.2 Laboratory Testing—Diffusion Measurements by the Electrical Conductivity Method

Diffusion of radionuclides in unsaturated gravel could occur very slowly on the solid mineral surface, through water in the interconnected porosity (present within the gravel grains), or through water films (present on the gravel surfaces). Previous research has indicated that diffusion through the water films is the most important mechanism (Conca and Wright 1990). Measuring low diffusion coefficients requires long duration measurements, the ability to sample on extremely small spatial scales, or an indirect approach. Calculating diffusion coefficients based on the electrical conductivity measurements is an indirect technique based on the Nernst-Einstein equation and has been accepted for diffusants in bulk aqueous samples (Conca and Wright 1992). If connected aqueous films in an unsaturated porous medium are the only

electrical-current-carrying pathway (assuming the conductivity of the mineral and open pore space is negligible), then a measurement of resistivity can be used to calculate a diffusivity. This method directly accounts for the tortuosity of the fluid pathway on the gravel surface and the diffusion resistance at inter-granular contacts.

The resistance of crushed tuff has been measured in a test cell with fixed geometry. The tuff was preconditioned with preset water contents, and the water contained a known concentration of potassium chloride. Diffusion coefficients were then calculated using the measured resistance and known geometry of the test cell. The inferred conductivity as a function of moisture content was plotted and compared to measurements by Conca and Wright (1992) and by others.

A test cell was constructed to contain tuff gravel, isolate the sample from the atmosphere, and apply four electrodes (Figure 20). The cell was constructed out of transparent PVC pipe with inside diameter of 6.225 cm (2.45 in.). Two stainless-steel screen electrodes were placed in the center of the cell approximately 65 mm (2.6 in.) apart. A sealable access port was placed between the two screen electrodes. Tuff samples (SPC 527451) from the middle nonlithophysal zone of the " Spring Tuff were collected, crushed, and sieved into various size fractions. The crushed tuff used in the measurements was from the 2- to 4-mm (0.07- to 0.16-in.) fraction of tuff sample with porosity and bulk density of 10.5 percent and 2.234 g/cm^3, respectively. Resistance measurements were made using a GenRad 1692 Digibridge LCR meter.

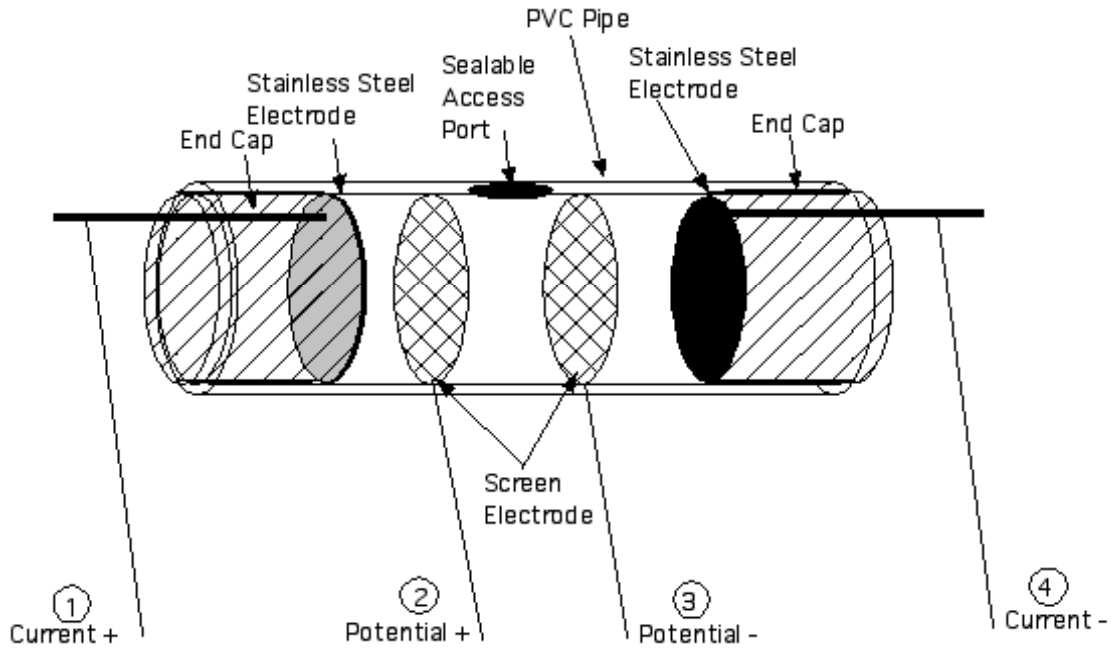

Figure 20. Measurement Cell

The crushed tuff was vacuum saturated in a 0.5-g/L KCl solution. The three compartments of the cell were filled with crushed tuff at the desired volumetric water content, ranging from cell saturation to less than 5 percent. Tuff was compacted into each of the cell compartments, and the porosity of each of the three compartments was assumed to be equal. High water contents were initially used (saturated and initial drainage), and these were attained by simply emplacing the saturated tuff in the cell with the saturating brine (0.5 g/L KCl) and draining the sample,

using a porous ceramic drain in the cell. Further tuff drainage was accomplished using an ultracentrifuge. Portions of the saturated tuff were placed in centrifuge cups and drained under specified conditions. Following the centrifugation, the tuff was placed into the cell inside a glove bag maintained at high relative humidity by a beaker of warm water. This was to prevent dryout of the surface layer of water on the tuff grains. After filling, the cell was placed into an incubator maintained at 22°C (72°F) for several hours to allow for thermal equilibration.

The diffusivities calculated using the Nernst–Einstein equation for volumetric moisture content are shown in Table 7. The five points with volumetric water content greater than 5.4 percent were attained by drainage of the initially brine-saturated cell. Volumetric water contents below 5.4 percent were achieved by centrifuging vacuum-saturated tuff at 1,000, 2,000, 3,000, 4,000, and 8,000 rpm in a Beckman L8-60M/P HT ultracentrifuge prior to placing it in the cell. The tuff appeared drier and drier as the centrifuge speed increased. Any handling of the tuff resulted in some breakage. Centrifugation at 8,000 rpm resulted in a high amount of smaller particles being generated (and a higher packing density in the cell).

Table 7. Diffusion Coefficients and Cell Conditions During Measurements

Tuff grain volumetric water content (cm^3/cm^3) [a]	0.945	0.194	0.118	0.118	0.118	0.114	0.104	0.103	0.097	0.098
Cell volumetric water content[b]	0.547	0.092	0.055	0.055	0.055	0.052	0.050	0.052	0.049	0.050
Inter-granular Porosity	0.494	0.494	0.494	0.494	0.494	0.539	0.517	0.495	0.494	0.487
D_{avg} (cm^2/s)	6.53E-06	3.46E-07	1.39E-07	1.48E-07	1.36E-07	5.27E-08	2.22E-08	2.03E-08	2.00E-08	1.24E-08

NOTES: [a]Calculated volumetric water content based on the crushed tuff bulk volume (=volume of water/total volume of tuff grains including intra-granular porosity). Values exceeding the grain porosity (0.105) indicate conditions beyond grain saturation.

[b]Calculated volumetric water content based on the cell volume (=volume of water/cell volume).

Figure 21 presents the comparisons of the calculated diffusion coefficients to the data from Conca and Wright (1990) and to the data presented in DTN MO9807SPA00026.000. The new measurements for diffusion coefficient are consistent with previously reported values used in the TSPA-SR and supplemental TSPA model analyses. As saturation decreased below about 5 percent, the diffusion coefficient began to decrease more sharply than at higher saturations. Only a limited part of the lower saturation range was accessible, experimentally, because as the centrifuge speed was increased, the volumetric water content declined only slightly on a tuff grain basis. These changes resulted in increases in measured resistance and decreases in the calculated diffusion coefficient, without any apparent decrease in volumetric water content on a cell basis. To address lower saturations, a dry, 2- to 4-mm (0.07- to 0.16-in.) crushed tuff sample was placed in a humidity chamber. The diffusion through this sample was below the detection limit.

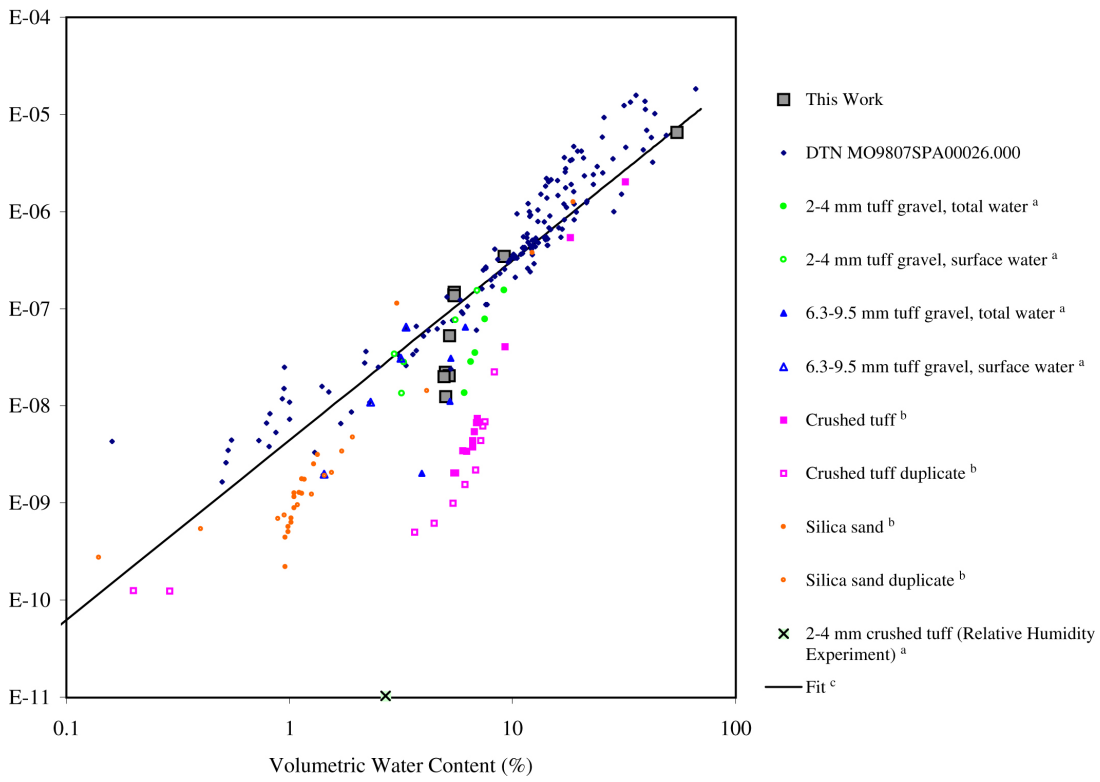

NOTES: [a]Conca 1990; [b]CRWMS M&O 2000c; [c]BSC 2001e.

Figure 21. Diffusion Coefficient Versus Volumetric Water Content for This and Other Work

These experimental results indicate the potential for low diffusivity values if the volumetric water content of the intra-granular medium is significantly less than its porosity. This condition is unlikely to occur in the invert as currently designed, since the crushed tuff and host rock have similar hydraulic properties.

An important aspect of the use of the Nernst–Einstein equation is that the mode of electrical conduction must be known. That is, to use the Nernst–Einstein equation to calculate diffusion coefficients in an aqueous system, there must be an understanding of the contribution to total electrical conduction from various possible modes of current conduction. If other modes of current conduction are present (such as through the mineral, on the dry mineral surface, through adsorbed water on the mineral surface, through the intra-granular pore space, or at the grain/grain connections), the Nernst–Einstein equation may not be applicable or these individual effects may require quantification. It has been shown that at low saturations, densely welded tuff has a significant surface conduction contribution to total electrical conduction (Roberts and Lin 1997).

Other concerns with this experimental technique are electrode design, electrode/sample polarization, and contact impedance at the electrode/sample interfaces. An attempt to assess the effects of electrode-contact impedance was made during this feasibility study by measuring with both a four-electrode configuration and multiple two-electrode configurations. When a four-electrode configuration was used, current was applied across the outer electrodes and potential

was measured across the inner electrodes. In the wires and electrodes, current is carried by electrons; in the water-rock system, current is carried by ions. This change in charge carrier from electronic to ionic occurring at the current electrode/rock interface results in contact impedance. The inner electrodes measure only the potential, and very little current is drawn from the system to make this measurement; thus, contact impedance at these electrodes leads to negligible voltage drop and is therefore unimportant. Calculating the resistance between the potential electrodes can then be accomplished without the influence of contact impedance. Using the two-electrode configuration, current was applied and potential was measured at the same two electrodes. Thus, any contact impedance was included in the resistance calculation. This contact impedance was minimal at high volumetric water contents but increased to as much as 5 percent of the indicated resistance in the drier measurements.

An additional problem with electrode-sample contact is that for the Nernst–Einstein equation to apply, a passive resistance (near-zero phase angle) is required. As the sample water content changed, the frequency providing the most passive resistance (smallest phase angle) also changed. For most of the two electrode measurements, 1,000 Hz was the best of the five frequencies available on the GenRad 1692. For the four electrode measurements, 100 and 120 Hz provided more passive resistance.

3.9.3 Laboratory Testing—Direct Diffusion Measurements by a Microprofiling Method

Laser ablation refers to the process in which an intense burst of energy delivered by a short laser pulse is used to vaporize a minute sample (in the range of nanograms) from a specific location. The chemical composition of the vaporized sample is then analyzed with inductively coupled plasma-mass spectrometry (ICP-MS). Laser ablation, coupled with ICP-MS (LA-ICP-MS), has recently evolved as a powerful analytical tool for solid samples (Russo et al. 2000). LA-ICP-MS can determine simultaneously a large number of chemical elements with very low detection limits. The high spatial resolution (in the range of microns) achieved by a focused laser beam makes LA-ICP-MS a very attractive investigative approach for slow diffusion processes. This section describes the method development, diffusion test design, and preliminary results using LA-ICP-MS.

A detailed feasibility study was conducted to evaluate the potential of the LA-ICP-MS approach to directly measure diffusion coefficients, both at rock surfaces and within rock matrix. This study included choosing appropriate tracers, probing elements intrinsic to tuff that can serve as internal standards to correct for different LA-ICP-MS conditions, evaluating surface profiling (moving the sampling point to the next location along the surface) and depth profiling (sampling deeper depths at the same location), and examining crater depths from certain laser pulses.

Figure 22 shows the crater shape and depth from laser ablation on tuff. The results indicate that the obtained spot size of the crater is consistent with the spot size chosen from the laser system. Furthermore, although the crater has a quite smooth bottom after 50 laser pulses, rougher profiles are obtained with fewer laser pulses, as expected. Crater depth is proportional to the number of laser pulses applied. This information provides confidence in correlating the number of laser pulses to the crater depth, i.e., sampling distance (during depth profiling) of tracer distribution for diffusion evaluation in rock matrix.

(A)

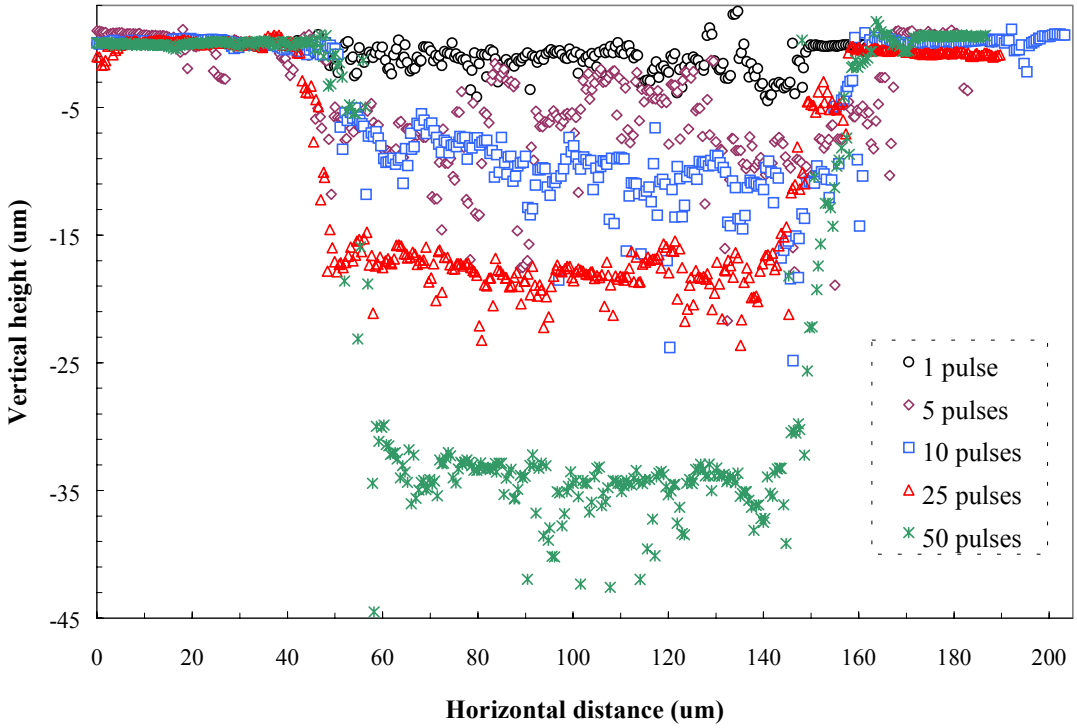

(B)

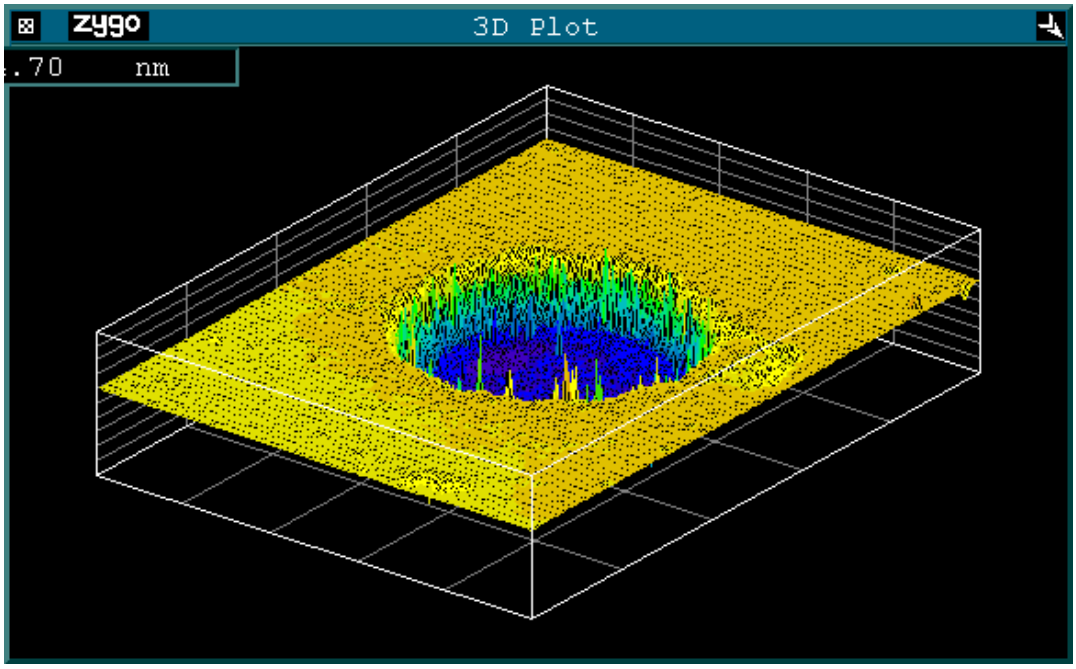

Figure 22. Crater Depth and Shape at a Nominal 100 µm Spot Size. (A) Surface profiles at different laser pulses. (B) Three-dimensional plot for 50 laser pulses.

A half-cell approach was used to prepare samples for diffusion evaluation using the LA-ICP-MS technique. In this approach, a tuff cube containing a tracer was placed in contact with a cube not containing the tracer, both under the same thermodynamic conditions (see Figure 23). The tracer then diffused from the tracer-containing cube to the other. Machined 1.5-cm (0.6-in.) tuff cubes were used in this feasibility study. Tracers were chosen based on their chemical similarity to radionuclides of interest. The source tuff cube was vacuum-saturated with a tracer solution that contained a mixture of NaBr, $NaReO_4$, CsBr, and RbBr. Both Br^- and perrhenate (ReO_4^-) act as nonsorbing tracers. Perrhenate serves as an analogue to technetium, which exists in a form of pertechnetate (TcO_4^-). Cesium (Cs^+) and rubidium (Rb^+) were used as cationic tracers to examine the delayed diffusive transport from chemical sorption and retardation. Nonradioactive Cs was used as a surrogate for radioactive ^{137}Cs. The sink tuff cube was also vacuum-saturated, but without tracers. Source and sink cubes were then separately placed inside a humidity chamber within an incubator maintained at 22°C (72°F). The high (near 100 percent) relative humidity was maintained by evaporation from free-standing water beakers inside the enclosed chamber. Cube weight was monitored over time until it reached a constant weight after 13 days. This pre-equilibration ensured establishment of similar water potential between source and sink cubes to prevent/minimize potential advection process. The cubes were then clamped together and left in the RH chamber to start the diffusion test.

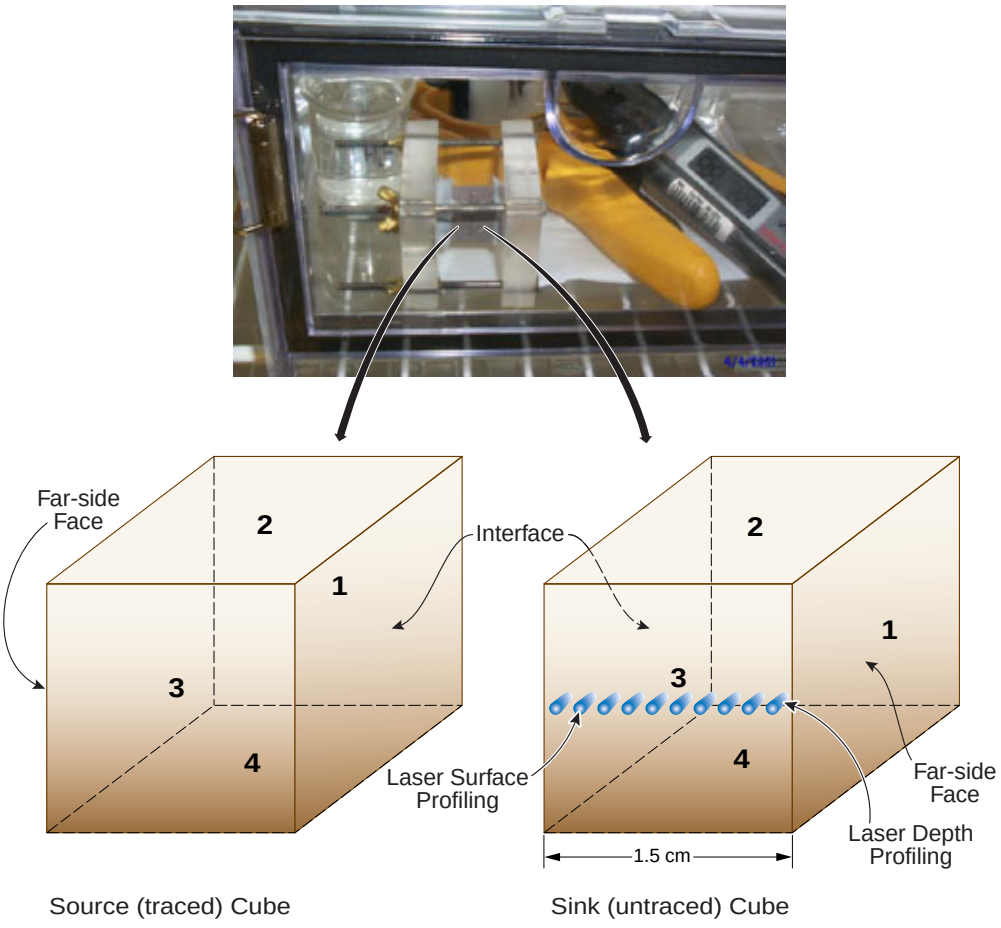

Figure 23. Half-cell Diffusion Experimental Setup and Schematics of Surface and Depth Profiling. Face designation is also indicated.

After 87 days, the diffusion test was stopped by separating the interface connection of source and sink cubes. The surface and depth tracer distributions were then mapped (Figure 24), using LA-ICP-MS. Figure 24 shows the tracer distribution and comparison for both the source and sink cubes. Nonsorbing tracers (ReO_4^- and Br^-) were present almost entirely across the sink cube face (Face 3) that is perpendicular to the interface face (i.e., in the direction of surface diffusion), which indicates rapid diffusion. Sorbing tracers (Cs^+ and Rb^+) traveled about 10 mm (0.4 in.) from the interface face as a result of their sorption onto the tuff matrix. (This behavior was also observed from the results obtained for other faces, as well as another diffusion test with a diffusion time of 150 days.) Tracer distribution was corroborated from the results on the far-side face of the sink cube, where nonsorbing tracers were detected while sorbing tracers were nearly at background levels. As expected, the tracer distributions on the far-side face of the source cube were more uniform, as well as at much higher concentrations than the diffusion faces. Furthermore, the interface side had a similar tracer concentration distribution for both the source and sink cubes.

The nonsorbing tracer, ReO_4^-, diffused through the surface water film at a rate similar to its aqueous diffusion in bulk water (on the order of 10^{-9} m^2/s). This is not surprising, considering that the tuff cubes were located in a high relative humidity chamber with the likely presence of a thick water film on the surfaces that behaves like bulk water. Furthermore, the half-cell design for the feasibility study was comprised of a cube–cube connection that maximizes contact between the source and the sink.

Laser profiling was also conducted depth-wise for the sink cube on Face 3. These results demonstrated that the tracer distribution decreases dramatically as the sampling depth increases (on the scale of microns), clearly indicating very slow diffusion inside the tuff matrix.

The one-dimensional analytical solution for diffusion into a semi-infinite media with a constant source (Crank 1975) was used to analyze the data:

$$C(x,t) = C_0 \text{ erfc } \{x/[2(D_e \times t)^{0.5}]\} \qquad (1)$$

where $C(x,t)$ (M L^{-3}) is the observed concentration based on an initial concentration C_0 (M L^{-3}), x (L) is the distance from the inlet boundary into the medium, t (T) is the time, and D_e (L^2 T^{-1}) is the effective diffusion coefficient of the diffusant in the medium. Because of unsaturated conditions, it was expected that the nonsorbing tracers such as ReO_4^- would be diffusively transported more slowly than in bulk aqueous solutions. Because of the somewhat linear profiles observed, however, the diffusion coefficients were only bounded for the conditions investigated.

To evaluate internal diffusion from the depth profile results, the measured signal was converted to a form of C/C_0 by treating the first depth measurement (two laser pulses with a depth about 4 μm) as the source concentration for each tracer. This conversion was conducted for all available depth profiling results. Figure 25 indicates that the internal diffusion coefficient for nonsorbing tracers is in the range of 10^{-16} m^2/s, which is nearly seven orders of magnitude lower than that of surface diffusion.

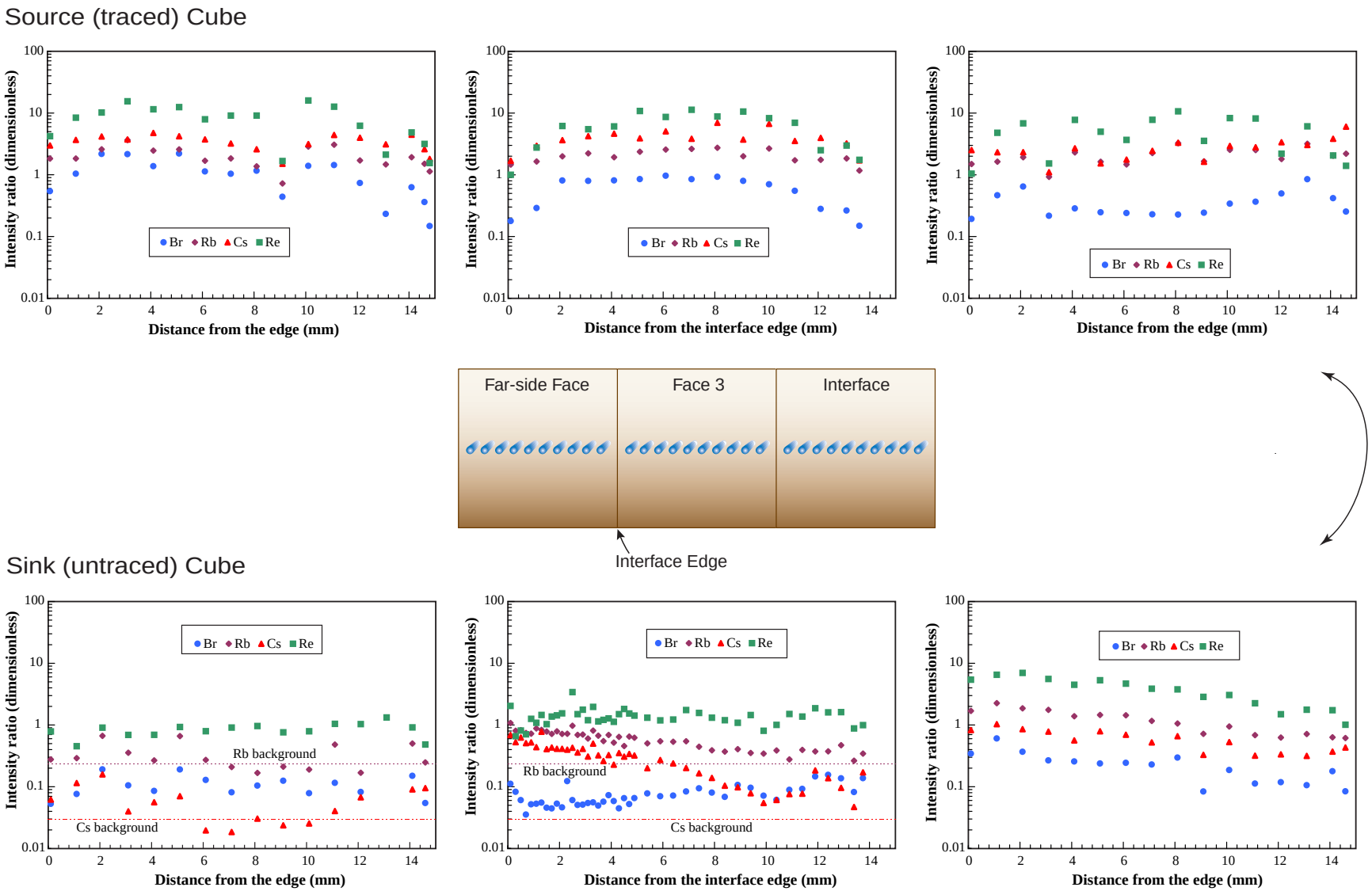

Figure 24. Tracer Distribution from Surface Profiling using LA-ICP-MS (100 µm spot size and 10 laser pulses). Y-axis: intensity ratio denotes the signal of each tracer divided by the signal of aluminum.

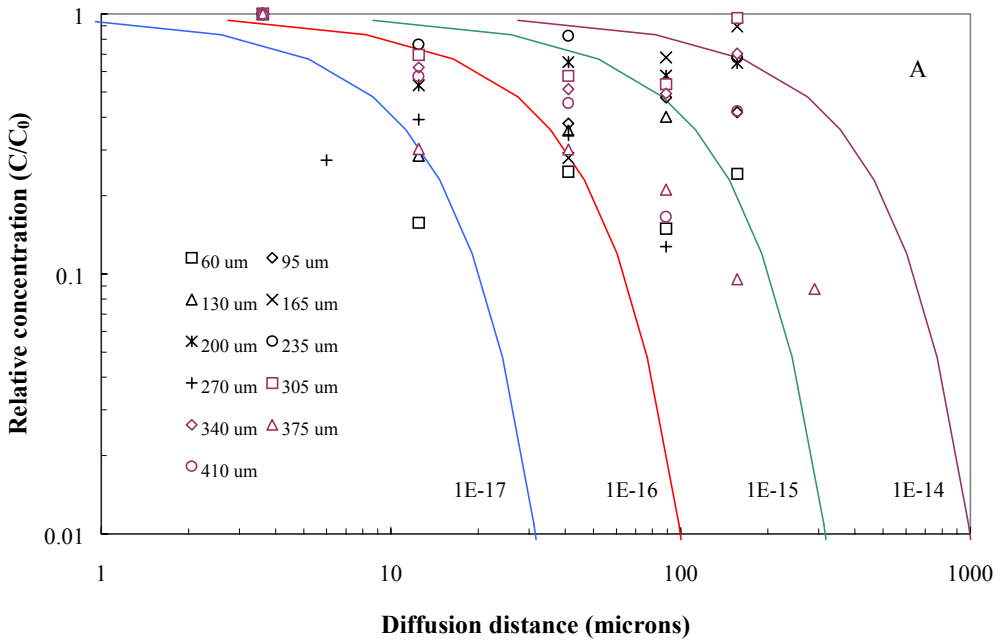

Figure 25. Tracer Distribution with Respect to Different Lateral Locations from the Interface (distances shown in the legend): (A) bromide; (B) perrhenate. Solid lines are obtained from one-dimensional analytical solution to diffusion (Equation 2), with the respective diffusion coefficients (m^2/s) presented on the plot.

3.10 EBS PHYSICAL AND CHEMICAL ENVIRONMENT MODEL

The principal objective of the *Engineered Barrier System: Physical and Chemical Environment Model* (BSC, in preparation [a]) is to represent the evolution of the physical and chemical conditions within the EBS emplacement drifts. This model is comprised of several conceptual and predictive submodels. The modeling approaches used, and in some cases the model output data, are intended for use in performance assessment as inputs to the performance of the EBS, the waste package, and the waste form.

Several updated EBS chemical environment submodels and analyses were introduced in the *FY01 Supplemental Science and Performance Analyses* (BSC 2001a). Extensive efforts were made since the *FY01 Supplemental Science and Performance Analyses* to validate models and document analyses in accordance with Project quality assurance procedures. This section summarizes these efforts.

3.10.1 Incoming Water and Gas Composition Abstraction

The initial boundary water and gas compositions used for in-drift chemistry modeling start with predictions of seepage water chemistry and gas-phase composition in the host rock (near field environment) adjacent to the drift wall. A discussion of the detailed model used to derive these compositions is presented in *Drift-Scale Coupled Processes (Drift Scale Test and THC Seepage) Models* (BSC 2001f). The results of this model are abstracted (i.e., simplified) to limit the

number of calculations needed by each of the models (described below) to capture the time- and temperature-dependent changes in drift boundary conditions. The abstraction analyses presented in the *FY01 Supplemental Science and Performance Analyses* (BSC 2001a) are documented in *EBS Incoming Water and Gas Composition Abstraction Calculations for Different Drift Temperature Environments* (BSC, in preparation [b]).

Using the updated thermal-hydrologic-chemical (THC) seepage model results, 16 abstraction tables (DTN MO0110SPAEBS13.038) were produced for seepage chemistry and in-drift gas composition, all of which reflect the mean infiltration rate of Yucca Mountain. The methodology used to produce the abstraction tables was documented in *EBS Incoming Water and Gas Composition Abstraction Calculations for Different Drift Temperature Environments* (BSC, in preparation [b], Section 6; DTN: MO0110SPAEBS13.038). The general basis for this abstraction is outlined in *Abstraction of Drift-Scale Coupled Processes* (CRWMS M&O 2000d). However, a slightly different methodology (BSC, in preparation [b], Section 5.1) was used to abstract the THC seepage model results that allows for better traceability to the direct THC seepage model result and maintains conservation of charge balance. In addition to the slightly different methodology, the original assumptions (CRWMS M&O 2000d) were updated to reflect the current approach. This methodology also expanded the abstraction periods and provides a post 100,000-year result based on ambient temperature condition calculations that are documented in the THC seepage model.

The main differences observed in these recent analyses compared to the TSPA-SR model and supplemental TSPA model are from the different initial water compositions used in the thermal-hydrologic-chemical seepage model.

3.10.2 In-Drift Microbial Communities Model

The in-drift microbial communities model (CRWMS M&O 2000e) is used to calculate the total biomass that can be produced from the degradation of EBS materials, using a comparative mass and energy limitations approach. In general, the in-drift microbial communities model uses constraints on the supply rates of the nutrients to build an idealized microbial composition, comprised of carbon, nitrogen, sulfur, and phosphorous in addition to the water components. These constraints are compared to the constraints based on redox energy available to supply microbial growth in the system. The smaller of the two constraints provides the overall growth limitation. Additional validation calculations for the in-drift microbial communities model were performed and documented in *In-Drift Microbial Communities Model Validation Calculations* (BSC 2001g).

Since the current in-drift microbial communities model (CRWMS M&O 2000e) and Volume 1 of *FY01 Supplemental Science and Performance Analyses* (BSC 2001a) were documented, additional modeling work has been completed. A set of input data (DTN: MO9909SPAMING1.003) that was key in determining the size of the possible microbial communities was unqualified. This unqualified data set was replaced with a new DTN (MO0106SPAIDM01.034) as documented in *Microbial Communities Model Parameter Calculations for TSPA/SR* (BSC 2001h). In this calculation, several inputs were updated and an impact evaluation was documented so that the next revision to the in-drift microbial communities model will not contain unverified inputs.

Since all the calculations in the current version of the in-drift microbial communities model were done using the unqualified data, an initial assessment was made of how much of an impact does the new data set have on the current results. In order to determine this, all of the model validation calculations documented in *In-Drift Microbial Communities* (CRWMS M&O 2000e, Sections 6.7.2 and 6.7.3) were rerun and documented in a calculation document entitled *In-Drift Microbial Communities Model Validation Calculations* (BSC 2001g). A comparison of the results of these two sets of model validation calculations indicates that there are fewer microbes (by a factor of 2) produced using the new DTN as opposed to the old DTN. Therefore, the results currently found in *In-Drift Microbial Communities* (CRWMS M&O 2000e) should still be bounding as the factor of two decrease falls within the one order of magnitude accuracy of the model. The additional calculations reported in *In-Drift Microbial Communities Model Validation Calculations* (BSC 2001g) uphold the conclusions for a valid model found in *In-Drift Microbial Communities* (CRWMS M&O 2000e, Section 7.3).

3.10.3 Microbial Sorption and Transport Model

A model for microbial sorption and transport was first presented in the *FY01 Supplemental Science and Performance Analyses* (BSC 2001a). This model is described and validated in *Engineered Barrier System: Physical and Chemical Environment Model* (BSC, in preparation [a]). In addition, *Microbial Transport Sensitivity Calculations* (BSC 2001i) documents a set of calculations performed to determine the magnitude of non-metabolic sorption of radionuclides by microbes and the potential release from the EBS of radionuclide-charged microbes as colloidal particles. As this model is designed to be implemented directly into a TSPA model, there are no directly calculated results. However, the results documented in *Microbial Transport Sensitivity Calculations* (BSC 2001i, Section 6) demonstrate that for the case where the concentration of U, Pu, and Th is greater than the uptake distribution and for a pH in the invert < 8, then the saturation of the invert controls the transfer of aqueous radionuclides onto microbes and also controls the release of microbial colloids to the UZ.

The mass of uranium sorbed onto the biomass was either sequestered in the EBS or transported as a microbial colloid based on a regression of data from Jewett et al. (1999), representing microbial sorption onto air-water interfaces in unsaturated column experiments. Over a period of one million years, it is estimated that EBS microbes may sequester from 77 to 2,302 kg of uranium per meter of waste package (up to about 100 percent of the inventory) depending on the saturation of the invert and type of waste package. Over the same time, microbial colloids may transport from 8 to 1,250 kg of uranium per meter of waste package (up to about 50 percent of the inventory).

The calculations noted above indicate microbial sorption of uranium will serve to reduce aqueous releases from the EBS by sequestration onto cell walls, whether they are living or non-living. These microbes will generally adhere to surfaces in the invert or to degraded waste package materials unless the water saturation of these materials is large enough to allow for the movement of the microbes as colloids. The net effect of the microbial sorption process is to transfer from 5 to 48 percent of the mass retained on microbial cell walls into the colloidal transport regime. The remainder of sorbed uranium will remain within the EBS. Thus, there could potentially be a net reductive effect on dose since 52 to 95 percent of all radionuclide mass sorbed onto microbes will not be transported out of the EBS as long as the pH remains below 8.

The key uncertainty in this model lies in the fact that once pH goes above 8 or an organism dies and is ultimately destroyed, desorption of uranium that has not precipitated as a uranium metal could occur. However, evidence suggests (Suzuki and Banfield 1999, pp. 406 to 407) that much of the uranium sorbed onto microbes is found in crystalline phases attached to the cell wall or encapsulated in the biofilm. This fact indicates that upon death the majority of the sorbed uranium may potentially remain as a reduced mineral phase.

3.10.4 In-Drift Precipitates and Salts Model

The precipitates/salts model is documented and validated in the *In-Drift Precipitates/Salts Analysis* (BSC, in preparation [c]). This model was developed to predict the effects of evaporation on formation of precipitated phases and water composition in order to provide estimates of pH, chloride concentration, and ionic strength to the total system performance model. In addition, based on the precipitated mineralogy, this model assesses the presence or absence of water within the EBS as a function of time, relative humidity, temperature, evaporation rate, and seepage rate. Several supplemental TSPA model analyses are documented in the following calculations:

- *In-Drift Precipitates/Salts Analysis* (BSC, in preparation [c])
- *Precipitates/Salts Model Results for THC Abstraction* (CRWMS M&O 2001b)
- *Precipitates/Salts Model Sensitivity Calculations* (BSC, in preparation [d])
- *Precipitates/Salts Model Calculations For Various Drift Temperature Environments* (BSC, in preparation [e])

Drift-Scale Coupled Processes (DST and THC Seepage) Models (BSC 2001f) provided an updated set of seepage compositions that were applied to the precipitates/salts model. These data were abstracted and were used as input to the precipitates/salts model calculations (BSC, in preparation [e]).

Figures 26 and 27 (Figures 6.4-1 and 6.4-2 in *Engineered Barrier System: Physical and Chemical Environment Model* [BSC, in preparation [a]]) show the effects of evaporation on the composition of the water and precipitates for the abstraction for seepage at the crown of the drift in the Tptpmn host rock unit. Each constituent is shown, although the model is validated only for pH, Cl, and ionic strength outputs. True ionic strength calculations are represented by *IS* in the legend of Figure 26. Similarly, *ISa* represents the ionic strength approximation used for the lookup tables and is calculated using Equation 4 in the *In-Drift Precipitates/Salts Analysis* (BSC, in preparation [c], Section 6.3.2).

The persistently high concentrations of Na and Cl relative to other constituents and the Na:Cl molar ratio (>1) are typical of the preclosure, boiling, extended cool-down, transition-to-ambient, and ambient periods of the THC seepage model abstractions (BSC 2001f). The early cool-down period, however, shows a tendency for a higher Cl concentration than Na. This is important because of the halite (NaCl) chemical divide.

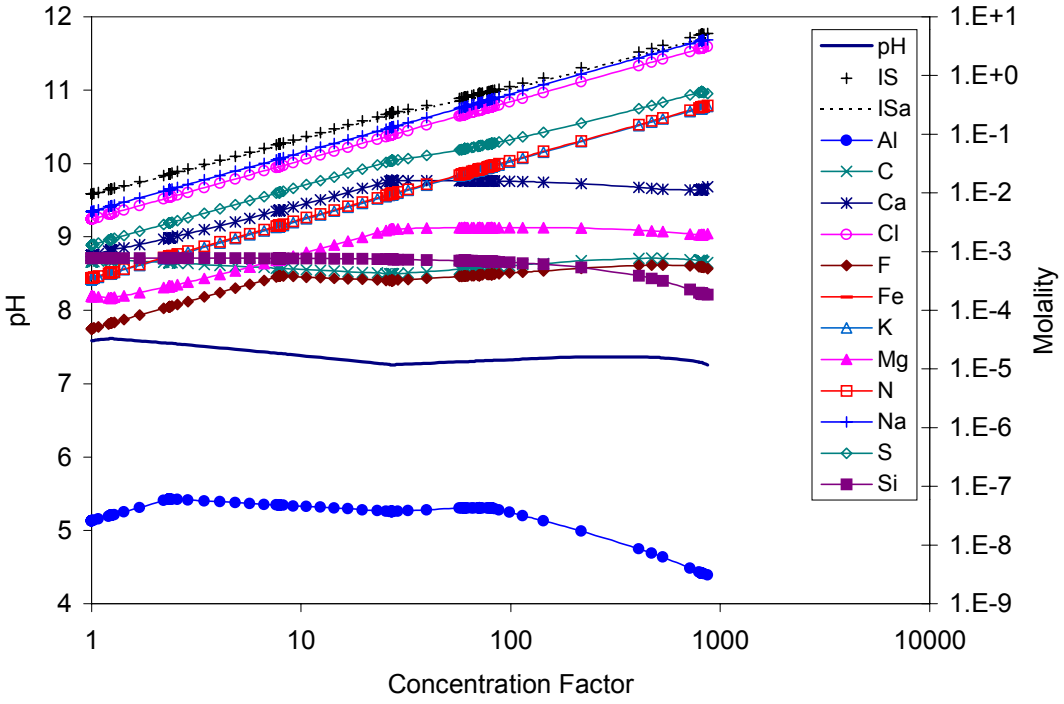

Figure 26. Aqueous Evaporative Evolution for the Base Case THC Model Abstraction for Seepage at the Crown of the Drift in the Tptpmn Lithology

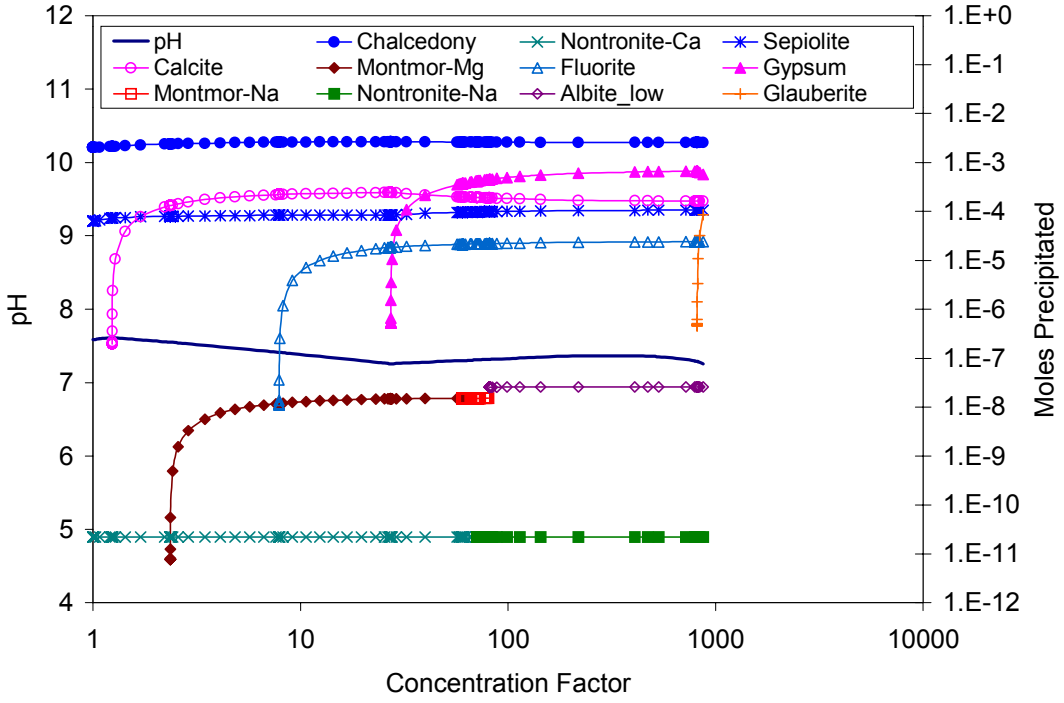

Figure 27. Mineral Evaporative Evolution for the Base Case THC Model Abstraction for Seepage at the Crown of the Drift in the Tptpmn Lithology

As described in the *In-Drift Precipitates/Salts Analysis* (BSC, in preparation [c]) and investigated in the *Precipitates/Salts Model Sensitivity Calculations* (BSC, in preparation [d]) and *Precipitates/Salts Model Calculations for Various Drift Temperature Environments* (BSC, in preparation [e]), the halite chemical divide will usually influence whether a chloride or sodium brine develops upon further evaporation. If halite reaches saturation and begins to precipitate, and the Na:Cl molar ratio is greater than one, then as evaporation continues, chloride becomes depleted in solution while excess sodium continues to concentrate. Conversely, if the ratio is less than one, then sodium becomes depleted while excess chloride continues to concentrate. This mechanism implies that a small difference in the original Na:Cl molar ratio can determine whether a sodium brine or a chloride brine develops beyond the halite chemical divide.

Evaporative evolution of most of the THC seepage model (BSC 2001f) abstraction waters favors the generation of sodium brines at the expense of chloride due to the Na:Cl molar ratios. This is also the case for the TSPA-SR abstractions. Early cool-down periods, however, favor the generation of chloride brines due to the elevated chloride concentrations relative to sodium in the seepage.

3.10.5 Acid-Neutralizing Capacity/pH Mixing Model

This model was first introduced in the *FY01 Supplemental Science and Performance Analyses* (BSC 2001a). The model mixes liquid (aqueous) fluxes from several sources to calculate the following variables for in-drift mixed solutions: ionic strength (I); pH, [Cl^-] and acid-neutralizing capacity, which is an indication of the solution's resistance to pH changes. Sources of liquid flux considered include seepage from the crown above the drift, the water wicked through the rock and corroded metals in the invert, and the diffusion film or flux from a waste package after failure. The acid-neutralizing capacity/pH mixing model is described and validated in *Engineered Barrier System: Physical and Chemical Environment Model* (BSC, in preparation [a]).

Preliminary analyses have been performed using the mixing model to examine a hypothetical case in which pH differences might be expected between the three different water sources entering the drift (waste package leachate, Topopah Spring Tuff fracture water [crown seepage], and "Topopah-Spring-Tuff-like pore water [invert wicking]) at about the 50,000-year time frame—as described in Section 6.7.2.9 in *Engineered Barrier System: Physical and Chemical Environment Model* (BSC, in preparation [a]). One important result from these analyses was that very large waste package leakage fluxes (1,251 kg/yr of water having a pH of 4) are required to substantially decrease the mixed solution pH below 7.0. Thus, water chemistry in the invert will tend to be controlled by evaporation in the invert and the chemistry of the waters entering the invert by crown seepage and capillary suction, rather than by the chemistry of the waste package leachate.

3.11 MODELING OF CEMENT-SEEPAGE INTERACTIONS

Additional modeling of interactions between percolating water and cement grout surrounding rock bolts is underway. These interactions can yield leachate with high pH and relatively high concentration of anions such as sulfate. The properties of the leachate are being predicted by developing a conceptual model of grout-seepage interactions and using geochemical modeling

software (EQ3/6) to predict the evolving water chemistry. Model validation is presented in *Engineered Barrier System: Physical and Chemical Environment Model* (BSC, in preparation [a]). Calculations are documented in *Seepage Grout Interaction Model Calculations* (BSC, in preparation [f]). The chemical composition of incoming seepage waters and carbon dioxide gas concentrations from the *EBS Incoming Water and Gas Composition Abstraction Calculations for Different Drift Temperature Environments* (BSC, in preparation [b]) were used as input. Additional input for sensitivity calculations was taken from evaporated seepage waters documented in *Precipitates/Salts Model Sensitivity Calculations* (BSC, in preparation [d]), which also used input water chemistries from *EBS Incoming Water and Gas Composition Abstraction Calculations for Different Drift Temperature Environments* (BSC, in preparation [b]).

The interaction of percolating water with cement grout can yield leachate with high pH and relatively high concentration of anions such as sulfate. To describe the effects of rock bolt use on waters seeping into the repository, the following conceptual model has been constructed to describe the system. Infiltrating seepage from unsaturated rock matrix and fractures percolates or imbibes into the cementitious rock bolt grout. The waters react with the grout mineralogy forming an alkaline leachate. The leachate percolates through the rock bolt grout to the crown of the drift where it forms a drip, which eventually falls to the drip shield below. The drip equilibrates with the drift partial pressure of carbon dioxide which has the effect of precipitating calcite and dropping the pH.

Two important conditions are assumed in this calculation:

1. Within the grout column, the system is closed with respect to gas phase carbon dioxide (i.e., carbon dioxide available in the grout is restricted to that which is dissolved in the influent water). This assumption forces the maximum leachate pH from the cement – water reaction.

2. Outside of the grout column, within the drift-air environment, the system is open with respect to gas phase carbon dioxide (i.e., the reaction is not limited by the availability of carbon dioxide). This assumption is reasonable given that the drift-air volume is essentially infinite compared to the surface area of the drift crown represented by rock bolt grout (i.e., it is not reasonable to assume that the reaction of leachate drips with in-drift gas could deplete the available carbon dioxide.

Goals for geochemical modeling of the system using EQ3/6 software are:

- Describe the chemistry of the potential waters percolating into the grout under different repository operating modes and time periods

- Describe the leachate chemistry formed by percolating water reacting with the grout

- Describe the resulting water chemistry after leachate reacts with drift-gas carbon dioxide

Both the cementitious grout and the incoming seepage water are characterized and provided as input to the EQ3/6 software. The grout is represented by a mineral assemblage that includes portlandite, ettringite, tobermorite, calcite, and brucite. The range of compositions of input

seepage water is provided in *Seepage Grout Interaction Model Calculations* (BSC, in preparation [f]).

Results of the geochemical modeling show that the leachate pH ranges from 10.1 to 12.4 for dilute incoming waters, and ranges from 10.3 to 13.2 for some of the high ionic strength evaporated incoming waters. The sensitivity of leachate formation to thermal operating mode and incoming water composition was also examined. Results indicate that cement leachate pH and composition strongly depend on temperature and to a much lesser extent, the quantity of dissolved carbon dioxide. The temperature of the abstracted incoming water strongly controls the solubilities of ettringite and portlandite, the primary cement mineral phases that control the pH of the leachate solutions. The solubility of ettringite increases with increasing temperature, and the solubility of portlandite decreases with increasing temperature. The simulation results also show that the highest pH leachates are created during the lower-temperature periods, and the lower-temperature operating mode creates the highest pH leachates for all repository periods.

Sensitivity to incoming water chemistry has also been explored in numerical simulations using differing incoming water chemistries including UZ-14 perched water, evaporated Alcove-5 pore water, evaporated perched water, and evaporated Drift Scale Test water. Results show that leachate pH and chemistry are relatively insensitive to incoming water composition, indicating that the dissolution of ettringite and portlandite are the important processes. The evaporated perched and Drift Scale Test waters produce the highest pH leachate (13.2) during lower-temperature repository periods. Due to the effects of carbon dioxide reactions with grout (carbonation reactions) and previous reaction of ettringite and portlandite, this effect will diminish over time. Note the main focus of this study is to determine the range of potential pH values and less so to determine how pH values change with time.

The reaction of cement leachate with the carbon dioxide in the drift air resulted in calcite precipitation and a subsequent decrease in solution pH. The resulting pH is strongly controlled by the partial pressure of carbon dioxide in the drift environment, with higher carbon dioxide partial pressure resulting in lower pH leachate. The leachates generated by low-ionic strength incoming water neutralize to pH values between 7.5 and 8.7, depending on the carbon dioxide partial pressure. Leachates generated by evaporated incoming waters neutralize to pH values ranging from 7.2 to 11.1. The high pHs are associated with the evaporated perched and Drift Scale Test waters. These waters enter the system with a high pH (8.4 to 11.1), and their buffering capacity limits the neutralization upon reaction with carbon dioxide in the drift air.

A sensitivity study was performed to evaluate the effect of evaporation on a water predicted to result from reaction with cement (BSC, in preparation [d]). The results of this study indicate that, after the cement leachate water is evaporated, its pH behavior will reflect the chemical composition of the original input water used to model the leaching reaction with cement.

3.12 ENHANCED CHARACTERIZATION OF THE REPOSITORY BLOCK CROSS-DRIFT BULKHEAD TEST RESULTS

The Cross-Drift of the Exploratory Studies Facility, referred to as the Enhanced Characterization of the Repository Block (ECRB) Cross-Drift, includes a section of drift over 800 m (2,600 ft) long that is unventilated. A series of three sequential bulkheads subdivide the region. Two

bulkheads were installed in June 1999, with a third installed in July 2000. Beyond the last bulkhead (furthest from the ventilated drift), the tunnel boring machine is parked, with standby power generating a small amount of heat. The results of the standby power are an increase in local rock temperatures. During five separate entries into the bulkheaded region, water was observed on the invert, the tunnel boring machine conveyer belt, and on sections of drift wall. Additional information about the chemistry of the water and the dryout of the near-field rock in the unheated and unventilated sections of the drift is included in Section 3.2 of the companion white paper for the unsaturated zone flow and transport process model.

A preliminary conclusion of the water chemistry measurements is that the water is not construction water and is much more dilute than seepage water that has equilibrated with the rock. One hypothesis is that the heat from the tunnel boring machine increased vapor pressure in the nearby rock, and that the vapor moved through the drifts and leaky bulkheads, or through the near-field rock to the cooler regions of the unventilated drift. The vapor then condensed directly in the drift or it condensed in nearby rock and then seeped into the drift. This situation is analogous to that of a heated emplacement drift (near the tunnel boring machine) and a nearby unheated perimeter drift following closure (the unventilated unheated region between the bulkheads). The analogy is not as strong for warmer and cooler sections of an emplacement drift, since the ECRB situation includes the coolest location between the bulkheads.

Preliminary consideration of the ECRB data, in conjunction with the modeling described in Sections 3.3 and 3.7, indicate:

- Natural convection tends to heat the upper parts of the drip shield more than the lower parts.
- Condensation occurs in cool regions.
- Barometric fluctuations propagating past or around the bulkheads may influence the condensation process.
- Most of the condensation driven by differences in heat sources will occur low in the drift footprint, near the drip shield toe, or on or beyond the drift walls.
- Most of the condensation will not contact the waste package surface or the waste form.
- The condensate may provide dilution to the contaminated effluent from waste packages such that precipitation of radionuclides due to declining temperatures may not occur until some distance from the drift, rather than in the invert.
- The magnitude of the condensation is largest during the thermal period in which no waste packages failed in TSPA-SR, and only one waste package failed in one-fourth of the realizations in the supplemental TSPA model.

4. IMPLICATIONS OF RECENT TEST RESULTS AND OTHER ADDITIONAL INFORMATION

Each of the subsections of Section 3 is interpreted below by the author, with respect to the significance of the additional data or modeling results to EBS performance. Overall, these interpretations are that the realism in the EBS models has increased since the *FY01 Supplemental Science and Performance Analyses* (BSC 2001a), and that uncertainties have been reduced. Further, model validation and documentation of some supplemental TSPA model results to full quality assurance procedures has increased confidence in the results.

4.1 EFFECTS OF ROCKFALL ON THE DRIP SHIELD AND WASTE PACKAGE

Rockfall on the drip shield during the first 10,000 years (before substantial strength loss due to corrosion) will not cause large-scale failure. Stress corrosion cracking subsequent to rockfall will produce a limited breach size in the drip shield with a potential design modification that stiffen the drip shield and increase the clearance between the it and the largest waste packages to preclude contact between a damaged drip shield and a waste package.

4.2 COMPARISON OF HEAT TRANSFER AND HEAT/MASS TRANFER MODELS FOR PRECLOSURE VENTILATION

The submodels implemented in the ANSYS and MULTIFLUX codes are consistent with analytic solutions of simplified situations. Refining the axial mesh implemented in the ANSYS code for the ventilation model results in preclosure temperatures similar to those reported in *FY01 Supplemental Science and Performance Analyses* (BSC 2001a). MULTIFLUX calculations using the ANSYS inputs, but accounting for latent heat cooling and dryout warming, are similar to ANSYS results at early preclosure times and locations near the drift entrance. The same MULTIFLUX calculations produce 5 to 10 C° (9 to 18 F°) warmer temperatures than the ANSYS results at later preclosure times and at distances farther into the drift.

4.3 COMPUTATIONAL FLUID DYNAMICS MODELING OF FORCED AND NATURAL CONVECTION IN SCALED TESTS AND AT REPOSITORY SCALE

The FLUENT computational fluid dynamics code results reasonably simulate scaled tests and agree with published correlations for idealized geometries.

4.4 RESULTS OF 25-PERCENT-SCALE FORCED VENTILATION TESTS

The tests are designed to validate the ventilation model. The ventilation efficiencies used in the TSPA-SR model (70 percent) and the supplemental TSPA model (70 percent for the HTOM, 80 percent for the LTOM) are similar to the 25-percent-scale test results. However, the test efficiencies are a function of both the ventilation heat transfer and the insulation design. The insulation was selected to simulate a larger volume of tuff rock; however, quantitative analyses to confirm the ventilation efficiency in TSPA models is valid are not yet complete. The flow rate in the TSPA-SR model and supplemental TSPA model is 15 m^3/s, and the powers are in the range covered in Table 5.

4.5 VALIDATION OF THE MULTISCALE THERMAL-HYDROLOGIC MODEL AND CORRECTIONS TO SUPPLEMENTAL TSPA MODEL RESULTS

Comparison of the MSTHM with a nested TH model demonstrated that the fundamental concept of combining multiple-location and multiple-scale submodels in the MSTHM is valid. This concept is to use multiple location-specific two-dimensional thermal-hydrologic (LDTH) submodels as the core of the model, and use three-dimensional mountain and drift scale thermal submodels to assemble and modify the LDTH results to include three-dimensional effects. One correction and one improvement to the supplemental TSPA model results were made based on the model validation results. Both changes to the MSTHM resulted in small changes to temperature and relative humidity (up to 6°C [11°F] and up to 5 to 10 percent in relative humidity).

4.6 THERMAL CONDUCTIVITY MODELING AND DATA AT LABORATORY AND FIELD SCALES

The field tests include the effects of lithophysae too large to be included in laboratory samples. Initial results from the field program (~1.7 W/m·K) are consistent with the range of thermal conductivities used in the supplemental TSPA model.

4.7 MODELING OF CONDENSATION ON EBS SURFACES

The effects of evaporation and condensation will reduce the waste-package-to-waste-package temperature variability and the larger scale variability between the repository edges and repository center. The rates of condensation in cooler sections of the drift could be comparable to host rock percolation flux at times shortly following closure and one to two orders of magnitude less than the host rock percolation flux at later times.

4.8 DUAL-PERMEABILITY MODELING OF THE INVERT

Results show that water from the surrounding host rock tends to move through and occupy the intra-granular (matrix) porosity whereas the inter-granular porosity acts as a capillary barrier. In addition, water fluxes through the intra-granular (matrix) porosity are not significantly sensitive to the variation in grain size. The current dual-permeability model calculations with the NUFT code cannot calculate the thickness of water films on the surfaces of the granular ballast, so they cannot at present be used to quantify the diffusion process through the intra-granular porosity. However, the single continuum approach in TSPA-SR model and the supplemental TSPA model, using measured diffusivities for samples of granular materials at varying moisture contents, remains a reasonable approach to determining radionuclide transport through the invert. These results are consistent with the recent experimental results described in Section 3.9.

4.9 IN-DRIFT DIFFUSION STUDY

Two experimental studies of diffusion processes in a porous granular material (tuff) provide insights into the importance of diffusion in water films on the surfaces of the granular ballast versus diffusion through the granular medium itself. The first experimental technique, based on an electrical conductivity analogue for diffusion, directly accounts for the tortuosity of the fluid pathway on the gravel surface and the diffusion resistance at inter-granular contacts. However, it

cannot distinguish between the surface and intra-granular diffusion processes, incorporates assumptions for the electrical conductivity analogue, and is susceptible to uncertainties from contact resistance between electrodes and the sample. The second experimental technique provides a direct measurement of diffusivity with a spatial resolution on the order of tens of microns for surface profiling and a few microns for depth profiling. The preliminary results from this microscale diffusion profiling work provide direct evidence and measurement of the surface and intra-granular diffusion. Measured values of the diffusivity with the electrical conductivity analogue are similar to the data from Conca and Wright (1990) and confirm the fit to the dependence of diffusivity versus moisture content used in TSPA. These results are consistent with the modeling results described in Section 3.8, whereby liquid water resides in or on the surface of the grains, and the inter-granular pore spaces are relatively free of liquid water.

4.10 ENGINEERED BARRIER SYSTEM PHYSICAL AND CHEMICAL ENVIRONMENT MODEL

Some supplemental models and analyses have been validated and documented in accordance with Project quality assurance procedures. Chemical environment submodel analyses completed since the *FY01 Supplemental Science and Performance Analyses* (BSC 2001a) are consistent with TSPA-SR model and supplemental TSPA model analyses except in two cases, the in-drift microbial communities model and the in-drift microbial sorption and transport model. In the former case, additional model validation calculations with qualified data indicate that fewer microbes may be produced than predicted previously for TSPA-SR. Therefore the TSPA-SR results should still be bounding.

In the latter case, calculations indicate microbial sorption of uranium will serve to reduce aqueous releases from the EBS by sequestration onto cell walls whether they are living or nonliving. These microbes will generally adhere to surfaces in the invert or on degraded waste package materials unless the water saturation of these materials is large enough to allow for the movement of the microbes as colloids. The net effect of the microbial sorption process is to transfer from 5 to 48 percent of the mass retained on microbial cell walls into the colloidal transport regime. The remainder of sorbed uranium will remain within the EBS. Thus, there could potentially be a net reduction radionuclide releases from the EBS since 52 to 95 percent of all radionuclide mass sorbed onto microbes will not be transported out of the EBS as long as the pH remains below 8. The key uncertainty in this model is that once pH goes above 8 or an organism dies and is ultimately destroyed, desorption of uranium that has not precipitated as a uranium metal could occur. However evidence suggests that much of the uranium sorbed onto microbes is found in crystalline phases attached to the cell wall or encapsulated in the biofilm. This fact indicates that upon death the majority of the sorbed uranium may potentially remain as a reduced mineral phase.

Finally, preliminary analyses of three different waters mixing in the invert (waste package leachate, Topopah Spring Tuff fracture water [crown seepage], and calculated Topopah Spring Tuff pore-like water [invert wicking]) indicate that, except for very large waste package leachate fluxes, the pH and ionic strength in the invert will be controlled by the water wicked into the invert by capillary suction or by calculated seepage water from the drift crown. Water chemistry in the invert for the TSPA-SR model was predicted using calculated drift crown seepage. Water chemistry in the invert for the supplemental TSPA model was predicted using Topopah Spring

Tuff pore-like water that was modified by different thermal operating temperatures and by different partial pressure of carbon dioxide boundary conditions. These waters cover the expected range of expected end-member chemistries, in which the former and latter waters tend to exhibit an increase and decrease in pH with evaporation, respectively.

4.11 MODELING OF CEMENT-SEEPAGE INTERACTIONS

Results show that leachate formation due to interactions between rock bolt grout and seepage may have pH values that range from approximately 7 to 12 for dilute incoming waters and approximately 7 to 13 for high ionic strength evaporated incoming waters. Leachate pH and chemistry are directly tied to the presence of portlandite and to a lesser extent ettringite. Simulation results also show that the results are temperature dependent and that the highest pH leachates are created during the lower-temperature periods. The uncertainty in these calculations is directly dependent on the availability of portlandite in the grout. Further, the amount of portlandite available in the system will decrease with time due to carbonation and utilization so that during the late periods the maximum pH values will eventually reduce to ambient values during the postclosure period. Finally, calculations indicate that after cement leachate water is evaporated, its pH behavior will tend to reflect the chemical composition of the original input water used to model the leaching reaction with cement.

4.12 ENHANCED CHARACTERIZATION OF THE REPOSITORY BLOCK BULKHEAD TEST RESULTS

The ECRB data, in conjunction with the modeling described in Sections 3.3 and 3.7, indicate most of the condensation will occur low in the drift and not contact the waste package surface or the waste form. The magnitude of the condensation is largest during the thermal period, which lasts a few thousand years. During the first 10,000 years, no waste packages failed in TSPA-SR, and only one waste package failed in one-fourth of the realizations in the supplemental TSPA model.

5. REFERENCES

AP-2.14Q, REV 2, ICN 0. *Review of Technical Products and Data.* Washington, D.C.: U.S. Department of Energy, Office of Civilian Radioactive Waste Management. ACC: MOL.20010801.0316.

AP-SIII.1Q, Rev. 0, ICN 1. *Scientific Notebooks.* Washington, D.C.: U.S. Department of Energy, Office of Civilian Radioactive Waste Management. ACC: MOL.20000516.0002.

Bishop, E.H. 1988. "Heat Transfer by Natural Convection of Helium Between Horizontal Isothermal Concentric Cylinders at Cryogenic Temperature." *Journal of Heat Transfer, Transactions of the ASME, 111,* 109–115. New York, New York: American Society of Mechanical Engineers.

BSC (Bechtel SAIC Company) 2001a. *FY01 Supplemental Science and Performance Analyses, Volume 1: Scientific Bases and Analyses.* TDR-MGR-MD-000007 REV 00 ICN 01. Las Vegas, Nevada: Bechtel SAIC Company. ACC: MOL.20010801.0404; MOL.20010712.0062; MOL.20010815.0001.

BSC 2001b. *Rock Fall on Drip Shield*. CAL-EDS-ME-000001 REV 01. Las Vegas, Nevada: Bechtel SAIC Company. ACC: MOL.20010713.0043.

BSC 2001c. Software Code: MULTIFLUX.V1.0. 10485-1.0-200100.

BSC 2001d. *In-Drift Thermal-Hydrological-Chemical Model*. ANL-EBS-MD-000026 REV 00 ICN 02. Las Vegas, Nevada: Bechtel SAIC Company. ACC: MOL.20010406.0012.

BSC 2001e. *Invert Diffusion Properties Model.* ANL-EBS-MD-000031 REV 01 ICN 01. Las Vegas, Nevada: Bechtel SAIC Company. ACC: MOL.20010801.0315.

BSC 2001f. *Drift-Scale Coupled Processes (DST and THC Seepage) Models*. MDL-NBS-HS-000001 REV 01 ICN 01. Las Vegas, Nevada: Bechtel SAIC Company. ACC: MOL.20010418.0010.

BSC 2001g. *In-Drift Microbial Communities Model Validation Calculations*. CAL-EBS-EV-000001 REV 00. Las Vegas, Nevada: Bechtel SAIC Company. ACC: MOL.20011016.0044.

BSC 2001h. *Microbial Communities Model Parameter Calculations for TSPA/SR*. CAL-EBS-PA-000001 REV 00. Las Vegas, Nevada: Bechtel SAIC Company. ACC: MOL.20010828.0002.

BSC 2001i. *Microbial Transport Sensitivity Calculations.* CAL-EBS-PA-000011 REV 00. Las Vegas, Nevada: Bechtel SAIC Company. ACC: MOL.20011015.0024.

BSC (in preparation [a]). *Engineered Barrier System: Physical and Chemical Environment Model*. ANL-EBS-MD-000033, REV 02. Las Vegas, Nevada: Bechtel SAIC Company.

BSC (in preparation [b]). *EBS Incoming Water and Gas Composition Abstraction Calculations for Different Drift Temperature Environments*. CAL-EBS-PA-000013 REV 00. Las Vegas, Nevada: Bechtel SAIC Company. Submit to RPC URN-0960

BSC (in preparation [c]). *In-Drift Precipitates/Salts Analysis*. ANL-EBS-MD-000045 REV 00 ICN 03. Las Vegas, Nevada: Bechtel SAIC Company. URN-0957

BSC (in preparation [d]). *Precipitates/Salts Model Sensitivity Calculations*. CAL-EBS-PA-000010 REV 00. Las Vegas, Nevada: Bechtel SAIC Company. URN-0955

BSC (in preparation [e]). *Precipitates/Salts Model Calculations for Various Drift Temperature Environments.* CAL-EBS-PA-000012 REV 00. Las Vegas, Nevada: Bechtel SAIC Company. URN-0956

BSC (in preparation [f]). *Seepage Grout Interactions Model Calculations*. CAL-EBS-PA-000014 REV 00. Las Vegas, Nevada: Bechtel SAIC Company.

Buscheck, T.A.; Gansemer, J.; Lee, K.H.; Sun, Y.; Mansur, K. and Glascoe, L. (in preparation). "Validation of the Multiscale Thermohydrologic Model Used for Analysis of a Repository at Yucca Mountain." (Submitted to *Journal of Contaminant Hydrology.*)

Carslaw, H.S. and Jaeger, J.C. 1959. *Conduction of Heat in Solids.* 2nd Edition. Oxford, Great Britain: Oxford University Press. TIC: 206085.

Conca, J.L. 1990. "Diffusion Barrier Transport Properties of Unsaturated Paintbrush Tuff Rubble Backfill." *High Level Radioactive Waste Management, Proceedings of the International Topical Meeting, Las Vegas, Nevada, April 8-12, 1990. 1,* 394-401. La Grange Park, Illinois: American Nuclear Society. TIC: 202058.

Conca, J.L. and Wright, J. 1990. "Diffusion Coefficients in Gravel Under Unsaturated Conditions." *Water Resources Research, 26,* (5), 1055-1066. Washington, D.C.: American Geophysical Union. TIC: 237421.

Conca, J.L. and Wright, J. 1992. "Diffusion and Flow in Gravel, Soil, and Whole Rock." *Applied Hydrogeology*, *1*, 5–24. Hanover, Germany: Verglalg Heinz Heise GmbH. TIC: 224081.

Crank, J. 1975. *The Mathematics of Diffusion*. 2nd Edition. Oxford, England: Clarendon Press. TIC: 9662.

CRWMS M&O (Civilian Radioactive Waste Management System Management and Operating Contractor) 1998. *Software Code: ANSYS. 5.4.* HP 30040 5.4.

CRWMS M&O 2000a. *Total System Performance Assessment for the Site Recommendation.* TDR-WIS-PA-000001 REV 00 ICN 01. Las Vegas, Nevada: CRWMS M&O. ACC: MOL.20001220.0045.

CRWMS M&O 2000b. *Rock Fall on Drip Shield.* CAL-EDS-ME-000001 REV 00. Las Vegas, Nevada: CRWMS M&O. ACC: MOL.20000509.0276.

CRWMS M&O 2000c. *The Determination of Diffusion Coefficient of Invert Materials*. TDR-EBS-MD-000002 REV 00. Las Vegas, Nevada: CRWMS M&O. ACC: MOL.20000124.0320.

CRWMS M&O 2000d. *Abstraction of Drift-Scale Coupled Processes*. ANL-BNS-HS-000029 REV 00. Las Vegas, Nevada: CRWMS M&O. ACC: MOL.20000525.0371.

CRWMS M&O 2000e. *In-Drift Microbial Communities*. ANL-EBS-MD-000038 REV 00 ICN 01. Las Vegas, Nevada: CRWMS M&O. ACC: MOL.20001213.0066.

CRWMS M&O 2001a. *Engineered Barrier System Features, Events, and Processes.* ANL-WIS-PA-000002 REV 01. Las Vegas, Nevada: CRWMS M&O. ACC: MOL.20010312.0024.

CRWMS M&O 2001b. *Precipitates/Salts Model Results for THC Abstraction*. CAL-EBS-PA-000008 REV 00 ICN 01. Las Vegas, Nevada: CRWMS M&O. ACC: MOL.20010125.0231.

DOE (U.S. Department of Energy) 2001a. *Yucca Mountain Science and Engineering Report*. DOE/RW-0539. Washington, D.C.: U.S. Department of Energy, Office of Civilian Radioactive Waste Management. ACC: MOL.20010524.0272.

DOE 2001b. *Yucca Mountain Preliminary Site Suitability Evaluation.* DOE/RW-0540. Washington, D.C.: U.S. Department of Energy, Office of Civilian Radioactive Waste Management. ACC: MOL.20011101.0082.

Fetter, C.W. 1993. *Contaminant Hydrogeology.* Upper Saddle River, New Jersey: Prentice Hall. TIC: 240691.

Hu, Q. and Wang, J.S.Y. (in preparation). "Diffusion in Unsaturated Geological Media: A Review." (Submitted to *Critical Reviews in Environmental Science and Technology*).

Jewett, D.G.; Logan, B.E.; Arnold, R.G.; and Bales, R.C. 1999. "Transport of *Pseudomonas fluorescens* Strain P17 through Quartz Sand Columns as a Function of Water Content." *Journal of Contaminant Hydrology*, *36*, (1-2), 73-89. New York, New York: Elsevier. TIC: 249653.

Kuehn, T.H. and Goldstein, R.J. 1976. "Correlating Equations for Natural Convection Heat Transfer Between Horizontal Circular Cylinders." *International Journal of Heat and Mass Transfer, 19,* (10), 1127-1134. New York, New York: Pergamon Press. TIC: 238411.

Kuehn, T.H. and Goldstein, R.J. 1978. "An Experimental Study of Natural Convection Heat Transfer in Concentric and Eccentric Horizontal Cylindrical Annuli." *Journal of Heat Transfer, Transactions of the ASME, 100,* (4), 635-640. New York, New York: American Society of Mechanical Engineers. TIC: 244433.

LB990861233129.001. Drift Scale Calibrated 1-D Property Set, FY99. Submittal date: 08/06/1999.

Lis, J. 1966. "Experimental Investigation of Natural Convection Heat Transfer in Simple and Obstructed Horizontal Annuli." *Proceedings of the Third International Heat Transfer Conference*, *4*, 196-204.

LLNL (Lawrence Livermore National Laboratory) 1999. *Software Code: NUFT V3.0s* V3.0s. 10088-3.0s-00.

LLNL 2000. *Software routine*: *XTOOL V10.1.* V10.1. Sun Ultra10. 10208-10.1-00.

MO0106SPAIDM01.034. Temperature Dependant Gibbs Free Energy Relationships for Selected Redox Half Reactions for Use in the In-Drift Microbial Communities Model. Submittal date: 06/19/2001. URN-0927

MO0110SPAEBS13.038. EBS Incoming Water and Gas Composition Abstraction Calculation Results. Submittal date: 10/16/2001.

MO9807SPA00026.000. Fitting of the Data for Diffusion Coefficient in Unsaturated Porous Media. Submittal date: 07/29/1998.

MO9909SPAMING1.003. Temperature Dependant Delta G Relationships for Selected Redox Half Reactions Used in MING V1.0. Submittal date: 09/14/1999.

Nitao, J.J. 1998. *Reference Manual for the NUFT Flow and Transport Code*, *Version 2.0*. UCRL-MA-130651. Livermore, California: Lawrence Livermore National Laboratory. TIC: 238072.

Roberts, J.J. and Lin, W. 1997. "Electrical Properties of Partially Saturated Topopah Spring Tuff: Water Distribution as a Function of Saturation." *Water Resources Research, 33,* (4), 577-587. Washington, D.C.: American Geophysical Union. TIC: 239736.

Russo, R.E.; Mao, X.; Borisov, O.V.; and Liu, H. 2000. "Laser Ablation in Atomic Spectroscopy." *Encyclopedia of Analytical Chemistry.* Meyers, R.A., ed. Pages 9485-9506. Chichester, England: John Wiley & Sons. TIC: 250479.

SNL (Sandia National Laboratories) 2001. *Software Code: FLUENT.* V5.5. 10550-5.5-00.

Suzuki, Y. and Banfield, J.F. 1999. "Geomicrobiology of Uranium." Chapter 8 of *Uranium: Mineralogy, Geochemistry and the Environment*. Burns, P.C. and Finch, R., eds. Reviews in Mineralogy Volume 38. Washington, D.C.: Mineralogical Society of America. TIC: 247121.